

Positron scattering and annihilation on noble gas atoms

D. G. Green,^{*} J. A. Ludlow,[†] and G. F. Gribakin[‡]

*Department of Applied Mathematics and Theoretical Physics,
Queen's University Belfast, Belfast BT7 1NN, Northern Ireland, UK*

Abstract

Positron scattering and annihilation on noble gas atoms below the positronium formation threshold is studied *ab initio* using many-body theory methods. The many-body theory provides a near-complete understanding of the positron-noble-gas-atom system at these energies and yields accurate numerical results. It accounts for positron-atom and electron-positron correlations, e.g., polarization of the atom by the incident positron and the non-perturbative process of virtual positronium formation. These correlations have a large effect on the scattering dynamics and result in a strong enhancement of the annihilation rates compared to the independent-particle mean-field description. Computed elastic scattering cross sections are found to be in good agreement with recent experimental results and Kohn variational and convergent close-coupling calculations. The calculated values of the annihilation rate parameter Z_{eff} (effective number of electrons participating in annihilation) rise steeply along the sequence of noble gas atoms due to the increasing strength of the correlation effects, and agree well with experimental data.

PACS numbers: 34.80.Uv, 78.70.Bj

* Address correspondence to dermot.green@durham.ac.uk;

Present address: Joint Quantum Centre (JQC) Durham/Newcastle, Departments of Chemistry & Physics, Durham University, South Road, Durham, DH1 3LE, UK.

† Present address: AquaQ Analytics, Forsyth House, Cromac Square, Belfast, BT2 8LA.

‡ g.gribakin@qub.ac.uk

I. INTRODUCTION

The scattering of low-energy positrons from noble gas atoms has been the subject of theoretical studies for many decades [1]. For an overview of the field of low-energy positron scattering, see the review [2]. Although the exchange interaction is absent, positron scattering from atoms is considerably more challenging to treat theoretically than the related problem of electron-atom scattering. For positrons, the static interaction with the atom is repulsive. At low positron energies this repulsion is cancelled by the attractive polarisation potential induced by the positron incident on the atom, leading to a delicate balance between the opposing potentials. A key role is thus played by positron-atom and positron-electron correlations. In addition, phenomena unique to positrons occur, namely, positronium formation (real or virtual) and positron annihilation.

Positronium (Ps) formation is a process in which a positron captures an atomic electron into a bound state. In positron-atom collisions it is usually the first inelastic scattering channel to open. This occurs when the positron energy exceeds the Ps-formation threshold, $\varepsilon_{\text{Ps}} = I + E_{1s}(\text{Ps}) = I - 6.8 \text{ eV}$, where I is the ionization potential of the atom, and usually has a pronounced effect on positron scattering [2]. It also affects the positron-atom interaction at energies below ε_{Ps} , where the Ps formation is *virtual*. Besides elastic scattering, another channel open at all positron energies is positron annihilation. For atomic and molecular targets the positron annihilation cross section is traditionally parameterised as $\sigma_a = \pi r_0^2 (c/v) Z_{\text{eff}}$, where r_0 is the classical electron radius, c is the speed of light, v is the incident positron velocity, and Z_{eff} is the effective number of electrons participating in the annihilation process. For $Z_{\text{eff}} = 1$ this formula gives the basic electron-positron annihilation cross section in the nonrelativistic Born approximation [3]. For many-electron targets Z_{eff} may naively be expected to be close to the number of electrons in the atom. However, the positron-atom interaction and electron-positron correlations have a strong effect on the annihilation rates [4, 5]. Experimental studies of positron annihilation in heavier noble gases yield Z_{eff} values that are orders of magnitude greater than those obtained in a simple static-field approximation [6, 7].

In this paper we use diagrammatic many-body theory to describe the interaction of positrons with noble gas atoms. Many-body theory allows one to fully quantify the role and magnitude of various correlation effects. Scattering phase shifts, differential and total

elastic scattering cross sections, and Z_{eff} are calculated *ab initio* with proper inclusion of the correlations [8]. Excellent agreement with experimental results and the results of other sophisticated theoretical approaches is found. This work, taken together with the many-body theory calculations of γ -spectra and rates for annihilation on core electrons of noble gases [9], forms a comprehensive study that provides a near-complete understanding of the positron-noble gas atom system at positron energies below the Ps-formation threshold.

Many-body theory [10] provides a natural framework for the inclusion of electron-electron and electron-positron correlations. It uses the apparatus of quantum field theory to develop a perturbative expansion for the amplitudes of various processes. The ability to show various contributions pictorially by means of Feynman diagrams makes the theory particularly transparent and helps one's intuition and understanding of many-body quantum phenomena. This theory is ideally suited to the problem of a particle interacting with a closed-shell atom, with successful applications to electron scattering from noble-gas atoms (see, e.g., Refs. [11–15]). The study of positron-atom scattering using the many-body theory thus should have been straightforward. However, progress in this direction was stymied by the difficulty in accounting for virtual Ps formation, as the Ps bound state cannot be accurately described by a finite number of perturbation terms. The need for this was realised early on [16], but a proper solution including summation of an infinite series of “ladder” diagrams was achieved only much later [17]. The effect of virtual Ps formation nearly doubles the overall strength of the positron-atom correlation attraction, as the terms in the series are of the same sign, leading to a large total. In contrast, in electron-atom scattering, such series is sign-alternating, giving a small, often negligible, overall contribution.

The first application of the many-body theory to positron scattering was for helium [16]. This study accounted for polarisation of the target by the positron and demonstrated the importance of virtual Ps formation by using a rather crude approximation (see also [18]). This approximation was also used in subsequent studies for helium and other noble-gas atoms [19, 20]. A more sophisticated approximation to the virtual Ps contribution was developed and applied to positron scattering, binding and annihilation in Refs. [21–24] (see also [25]). It was later used to calculate real Ps formation in noble-gas atoms [26] and produced mixed results. The complete evaluation of the ladder-diagram series was implemented in the positron-hydrogen study [17] which used B-spline basis sets to discretize the positron and electron continua. This approach has since been applied to positron binding

to the halogen negative ions [27], to positron scattering and annihilation on hydrogen-like ions [28], to the calculation of gamma-ray spectra for positron annihilation on the core and valence electrons in atoms [9, 29] and in molecules [30]. Another many-body theory technique that allows one to sum the dominant series of diagrams to all orders is the linearized coupled-cluster method which was used to calculate positron-atom bound states for a large number of atoms [31, 32].

Recently, a series of high-quality experimental measurements and convergent close-coupling (CCC) calculations have been performed for low-energy positron scattering along the noble gas sequence [33–40]. In the light of these new data, the many-body theory approach developed by the authors is applied here to a thorough study of positron interaction with the noble gas atoms.

The rest of the paper is organized as follows. In Secs. II and III we describe the many-body theory and the numerical implementation of this theory. In Sec. IV we present results for phase shifts, elastic scattering cross-sections, differential cross sections, energy resolved Z_{eff} and thermally averaged Z_{eff} and compare to existing experimental and theoretical data. Finally we conclude with a brief summary and outlook for future work. Algebraic expressions for the many-body diagrams are provided in Appendix A and tabulated numerical results are in Appendix B. We use atomic units (a.u.) throughout, unless stated otherwise.

II. MANY-BODY THEORY

A. Dyson equation and self-energy

The many-body theory description of a positron interacting with an atom is based on the Dyson equation (see, e.g., Ref. [41]),

$$(H_0 + \Sigma_\varepsilon)\psi_\varepsilon = \varepsilon\psi_\varepsilon, \quad (1)$$

where ψ_ε is the (quasiparticle) wavefunction of the positron, H_0 is the zeroth-order Hamiltonian of the positron in the static field of the atom (usually described in the Hartree-Fock (HF) approximation), ε is the positron energy and Σ_ε is a nonlocal energy-dependent correlation potential. This potential is equal to the self-energy of the single-particle Green's function of the positron in the presence of the atom [42]. It incorporates all the many-body

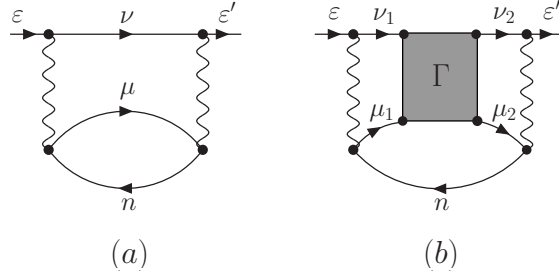


FIG. 1. Main contributions to the positron self-energy Σ_ε . The lowest, second-order diagram (a), $\Sigma_\varepsilon^{(2)}$, describes the effect of polarization; diagram (b), $\Sigma_\varepsilon^{(\Gamma)}$, accounts for virtual Ps formation represented by the Γ -block. Top lines in the diagrams describe the incident positron. Other lines with the arrows to the right are excited electron states, and to the left, holes, i.e., electron states occupied in the target ground state. Wavy lines represent Coulomb interactions. Summation over all intermediate positron, electron and hole states is assumed.

dynamics of the positron-atom system. As the potential Σ_ε is nonlocal, Dyson's equation is an integral equation,

$$H_0\psi_\varepsilon(\mathbf{r}) + \int \Sigma_\varepsilon(\mathbf{r}, \mathbf{r}')\psi_\varepsilon(\mathbf{r}')d\mathbf{r}' = \varepsilon\psi_\varepsilon(\mathbf{r}). \quad (2)$$

The correlation potential Σ_ε can be evaluated as an infinite perturbation series in powers of the residual electron-electron and electron-positron interactions. Because of the spherical symmetry of the atomic potential, Eq. (2) can be solved separately for each partial wave of the incident positron.

The main contribution to the positron self-energy Σ_ε is given by the two diagrams shown in Fig. 1. The second of these in fact represents an infinite subsequence of diagrams which describe virtual Ps formation. For a positron interacting with a one-electron target (the hydrogen atom or hydrogen-like ion), the diagrams shown in Fig. 1 constitute a complete expansion of Σ_ε . The algebraic expressions for these diagrams can be found in [17].

Diagram 1(a), $\Sigma_\varepsilon^{(2)}$, accounts for the polarisation of the atom by the positron. At large positron-atom separations this diagram has the asymptotic behaviour,

$$\Sigma_\varepsilon^{(2)}(\mathbf{r}, \mathbf{r}') \approx -\frac{\alpha_d e^2}{2r^4} \delta(\mathbf{r} - \mathbf{r}'), \quad (3)$$

where α_d is the static dipole polarisability of the atom (here, in the HF approximation). This second-order diagram (with its exchange counterparts) is known to provide a good ap-

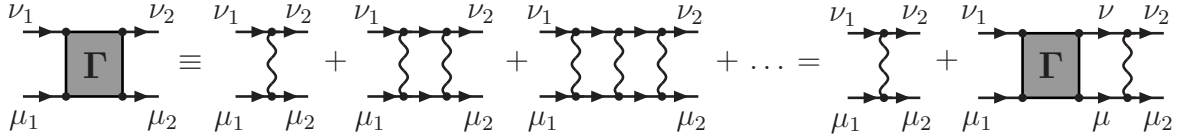


FIG. 2. Electron-positron ladder diagram series and its sum, the vertex function Γ (shaded block). Comparison between the left- and right-hand sides of the diagrammatic equation shows that Γ can be found by solving a linear matrix equation, Eq. (4).

proximation for Σ_ε in electron-atom scattering (e.g., for argon [13] or xenon [14]). However, the same approximation in positron-atom scattering is seriously deficient [16, 25].

Diagram 1(b), which we denote $\Sigma_\varepsilon^{(\Gamma)}$, describes the short-range attraction between the positron and the atom due to virtual Ps formation. The shaded Γ -block represents the sum of electron-positron ladder diagrams, referred to as the vertex function. It satisfies a linear integral equation represented diagrammatically in Fig. 2 and written in the operator form as

$$\Gamma = V + V\chi\Gamma, \quad (4)$$

where Γ is the vertex function, V is the electron-positron Coulomb interaction and χ is the propagator of the intermediate state. With the electron and positron continua discretised as described in Sec. III, Γ and V become matrices, with χ being a diagonal matrix of energy denominators, and the linear matrix equation Eq. (4) is easily solved numerically [17].

In order to describe the polarisation of multi-electron atoms more accurately, a set of third-order diagrams is also included in the calculation of Σ_ε . These diagrams, denoted collectively $\Sigma_\varepsilon^{(3)}$, are shown in Fig. 3. Algebraic expressions for these diagrams are given in Appendix A. Diagrams 3(a), (b), (c) and (d) represent corrections to the second-order polarization diagram Fig. 1(a) due to electron correlations of the type described by the random-phase approximation with exchange [43]. They account for the electron-hole interaction and screening of the positron and electron Coulomb field. Diagram 3(e) describes the positron-hole repulsion.

Instead of computing the self-energy $\Sigma_\varepsilon(\mathbf{r}, \mathbf{r}')$ in the coordinate representation, it is more

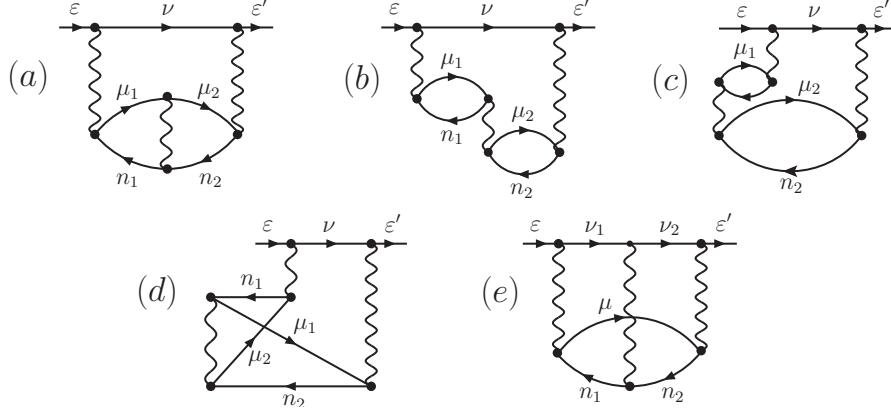


FIG. 3. Third-order correction diagrams, $\Sigma_\varepsilon^{(3)}$. Mirror images of the diagrams (c) and (d) are also included. In all diagrams the top, horizontal lines represent the positron.

convenient to deal with its matrix elements

$$\langle \varepsilon' | \Sigma_E | \varepsilon \rangle = \int \varphi_{\varepsilon'}^*(\mathbf{r}') \Sigma_E(\mathbf{r}', \mathbf{r}) \varphi_\varepsilon(\mathbf{r}) d\mathbf{r} d\mathbf{r}', \quad (5)$$

with respect to the zeroth-order static-field positron wavefunctions φ_ε with a given orbital angular momentum ℓ . They are eigenstates of the zeroth-order Hamiltonian,

$$H_0 \varphi_\varepsilon = \varepsilon \varphi_\varepsilon, \quad (6)$$

which satisfy the correct boundary conditions and are appropriately normalised. For true continuous-spectrum positron states we use normalisation of the radial wavefunctions to a δ -function of energy in Rydberg, $\delta(k^2 - k'^2)$. This corresponds to the asymptotic behaviour $P_{\ell}^{(0)}(r) \simeq (\pi k)^{-1/2} \sin(kr - \ell\pi/2 + \delta_\ell^{(0)})$, where $\delta_\ell^{(0)}$ are the static HF-field phase shifts, and k is the wavenumber related to the positron energy by $\varepsilon = k^2/2$. The intermediate states in the diagrams are square-integrable electron and positron basis functions – eigenstates of H_0 constructed from B-splines in a finite-size box of radius R (see Sec. III A).

B. Scattering phase shifts

The self-energy matrix (5) can be used to obtain the phaseshifts directly [43, 44]. First, a “reducible” self-energy matrix $\langle \varepsilon' | \tilde{\Sigma}_E | \varepsilon \rangle$ is found from the integral equation,

$$\langle \varepsilon' | \tilde{\Sigma}_E | \varepsilon \rangle = \langle \varepsilon' | \Sigma_E | \varepsilon \rangle + \mathcal{P} \int \frac{\langle \varepsilon' | \tilde{\Sigma}_E | \varepsilon'' \rangle \langle \varepsilon'' | \Sigma_E | \varepsilon \rangle}{E - \varepsilon''} d\varepsilon'', \quad (7)$$

where \mathcal{P} denotes the principal value of the integral. The phase shift is then given by,

$$\delta_\ell(k) = \delta_\ell^{(0)}(k) + \Delta\delta_\ell(k), \quad (8)$$

where

$$\tan [\Delta\delta_\ell(k)] = -2\pi \langle \varepsilon | \tilde{\Sigma}_\varepsilon | \varepsilon \rangle, \quad (9)$$

determines the additional phase shift $\Delta\delta_\ell(k)$ due to positron-atom correlations described by the self-energy.

The reducible self-energy matrix also allows one to find the positron quasiparticle wavefunction (i.e., solution to the Dyson equation), as

$$\psi_\varepsilon(\mathbf{r}) = \varphi_\varepsilon(\mathbf{r}) + \mathcal{P} \int \varphi_{\varepsilon'}(\mathbf{r}) \frac{\langle \varepsilon' | \tilde{\Sigma}_\varepsilon | \varepsilon \rangle}{\varepsilon - \varepsilon'} d\varepsilon'. \quad (10)$$

Numerically, the integrals in Eqs. (7) and (10) are calculated using an equispaced positron momentum of 200 intervals of $\Delta k = 0.02$. In order for the quasiparticle radial wavefunction to be correctly normalised and have the asymptic behaviour

$$P_{\varepsilon\ell}(r) \simeq \frac{1}{\sqrt{\pi k}} \sin \left(kr - \frac{\ell\pi}{2} + \delta_\ell^{(0)} + \Delta\delta_\ell \right), \quad (11)$$

the wavefunction from Eq. (10) must be multiplied by the factor,

$$\cos \Delta\delta_\ell = \left[1 + (2\pi \langle \varepsilon | \tilde{\Sigma}_\varepsilon | \varepsilon \rangle)^2 \right]^{-1/2}. \quad (12)$$

C. Positron annihilation

The annihilation rate λ for a positron in a gas of atoms (or molecules) with number density n is usually parameterised by

$$\lambda = \pi r_0^2 c n Z_{\text{eff}}, \quad (13)$$

where r_0 is the classical radius of the electron, c is the speed of light, and Z_{eff} is the effective number of electrons that participate in the annihilation process [4, 45]. In general the parameter Z_{eff} is different from the number of electrons in the target atom, Z . In particular, as we shall see, positron-atom and electron-positron correlations can make $Z_{\text{eff}} \gg Z$.

Theoretically, Z_{eff} is equal to the average positron density at the locations of the atomic electrons, i.e.,

$$Z_{\text{eff}} = \sum_{i=1}^N \int \delta(\mathbf{r} - \mathbf{r}_i) |\Psi_{\mathbf{k}}(\mathbf{r}_1, \dots, \mathbf{r}_N; \mathbf{r})|^2 d\mathbf{r}_1 \dots d\mathbf{r}_N d\mathbf{r}, \quad (14)$$

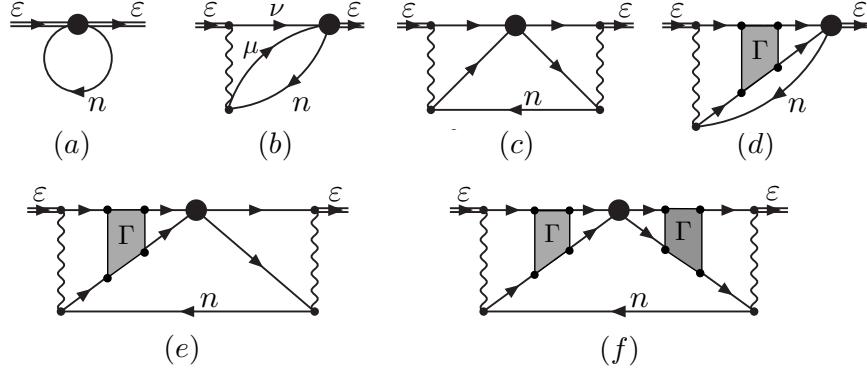


FIG. 4. Many-body theory expansion for Z_{eff} . The solid circle in the diagrams is the δ -function annihilation vertex, see Eq. (14). The double lines represent the fully correlated (Dyson) positron quasiparticle wavefunction of Eq. (10), i.e., the HF positron wavefunction ‘dressed’ with the positron self-energy in the field of the atom. Diagrams (b), (d) and (e) are multiplied by two to account for their mirror images.

where $\Psi_{\mathbf{k}}(\mathbf{r}_1, \dots, \mathbf{r}_N; \mathbf{r})$ is the total wavefunction which describes the scattering of the positron with momentum \mathbf{k} by the N -electron target atom. This wavefunction is normalised at large positron-atom separations to the positron plane wave incident on the ground-state target with the wavefunction Φ_0 :

$$\Psi_{\mathbf{k}}(\mathbf{r}_1, \dots, \mathbf{r}_N; \mathbf{r}) \simeq \Phi_0(\mathbf{r}_1, \dots, \mathbf{r}_N) e^{i\mathbf{k}\cdot\mathbf{r}}. \quad (15)$$

Equation (14) has the form of an amplitude, with the electron-positron delta-function acting as a perturbation. Hence, it is possible to derive a diagrammatic expansion for Z_{eff} [17, 25, 26]. Figure 4 shows the set of main annihilation diagrams. In addition to the elements found in the self-energy diagrams, these diagrams contain the electron-positron δ -function vertex. The diagrams in Fig. 4 provide a complete Z_{eff} for a one-electron system, such as hydrogen and hydrogen-like ions [28]. Algebraic expressions for these diagrams can be found in [17]. The simplest diagram, Fig. 4(a), is the zeroth-order (independent-particle) approximation,

$$Z_{\text{eff}}^{(0)} = \sum_{n=1}^N \int |\varphi_n(\mathbf{r})|^2 |\psi_\varepsilon(\mathbf{r})|^2 d\mathbf{r}, \quad (16)$$

represents the overlap of the positron and electron single-particle densities (φ_n being the n th HF electron ground-state orbital).

For the many-electron systems considered here, it is also important to account for electron screening in the calculation of Z_{eff} . A series of annihilation diagrams with two Coulomb interactions, similar to the self-energy corrections in Fig. 3, are therefore included, see Fig. 5. The corresponding algebraic expressions are given in Appendix A.

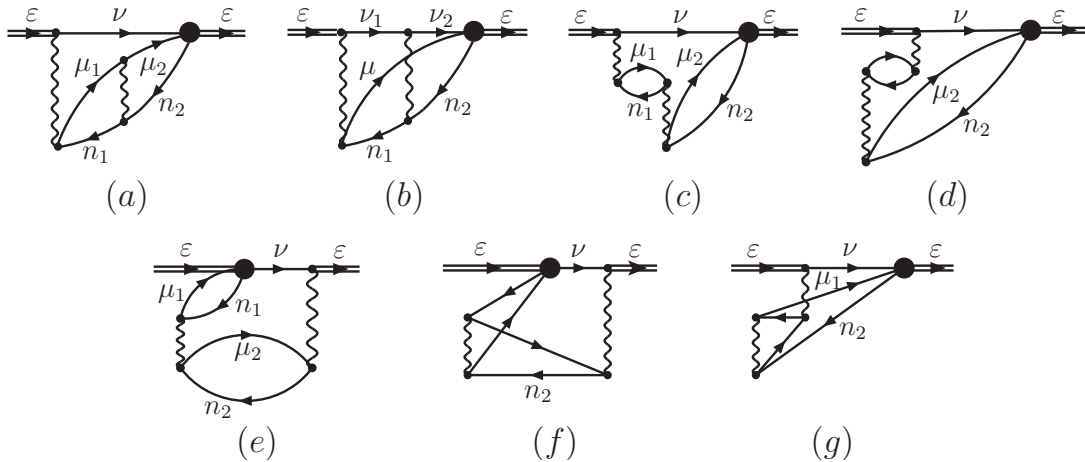


FIG. 5. Annihilation diagrams which account for corrections to Z_{eff} due to electron screening, electron-hole and positron-hole interactions. The top, horizontal lines represent the positron. The double lines represent the fully correlated (Dyson) positron quasiparticle wavefunction of Eq. (10). All the diagrams have equal mirror images.

The external lines in the Z_{eff} diagrams represent the wavefunction of the incident positron. In the lowest approximation, one can use the positron wavefunction in the static field of the HF ground-state atom, i.e., set $\psi_\varepsilon = \varphi_\varepsilon$, neglecting the effect of the correlation potential Σ_ε on the positron. This effect is in fact quite strong, so to obtain accurate Z_{eff} one needs to use the quasiparticle positron wavefunction of Eq. (1). Figures 4 and 5 represent the latter case, with double lines corresponding to the fully correlated (Dyson) positron quasiparticle wavefunction obtained from Eq. (10), i.e., the HF positron wavefunctions ‘dressed’ with the positron self-energy in the field of the atom (see Figs. 1 and 3), and normalised by the factor (12).

In order to implement the correct normalisation of the incident positron wavefunction to the plane wave $e^{i\mathbf{k}\cdot\mathbf{r}}$ at large distances, it is necessary to multiply the Z_{eff} diagrams computed

for the positron wavefunction with angular momentum ℓ , by

$$\frac{4\pi^2}{k}(2\ell + 1). \quad (17)$$

III. NUMERICAL IMPLEMENTATION

Below we outline the numerical implementation of the many-body theory methods described in Sec. II.

A. B-spline basis

First, the Hartree-Fock ground state of the atom is calculated with a standard HF package [46]. Using these numerical wavefunctions, direct and exchange potentials are constructed and the atomic HF Hamiltonian for the positron (i.e., without exchange) or electron (with exchange) is then diagonalised in a B-spline basis [47, 48]. The corresponding eigenvectors are used to construct the positron and electron wavefunctions. This provides effectively complete sets of positron and electron basis states covering both bound states and the energy continuum [17, 28]. These are then used to evaluate the sums over intermediate electron and positron states required in the evaluation of the many-body diagrams.

For the calculations carried out here a set of 40 splines of order 6 was used with a box size $R = 30$ a.u. Two outermost subshells are included when calculating the self-energy and annihilation diagrams. The many-body diagrams are evaluated at 8 energy points from zero incident positron energy up to the Ps formation threshold and then interpolated onto the required energies.

There is a point concerning boundary conditions satisfied by the B-spline basis states that affects the calculation of the self-energy matrix $\langle \varepsilon' | \Sigma_E | \varepsilon \rangle$. The self-energy matrix is evaluated initially using the B-spline basis states $|i\rangle$ as $\langle i | \Sigma_E | j \rangle$. The number of B-spline basis states used in each partial wave (~ 15) is much smaller than the number of continuous spectrum states required for an accurate solution of Eq. (7). The change to $\langle \varepsilon' | \Sigma_E | \varepsilon \rangle$ can be made using the effective completeness of the B-spline basis on the interval $[0, R]$,

$$\langle \varepsilon' | \Sigma_E | \varepsilon \rangle = \sum_{ij} \langle \varepsilon' | i \rangle \langle i | \Sigma_E | j \rangle \langle j | \varepsilon \rangle, \quad (18)$$

where $\langle \varepsilon | i \rangle$ is the overlap of the HF state ε with the B-spline basis state $|i\rangle$. However, unlike the B-spline states which satisfy the boundary condition $P_{i\ell}(R) = 0$, the continuous spectrum radial wave function $P_{\varepsilon\ell}(r)$ is finite at the boundary $r = R$. To improve numerical accuracy, a weighting function $f(r) = R - r$ is inserted into Eq. (18):

$$\langle \varepsilon' | \Sigma_E | \varepsilon \rangle = \sum_{ij} \langle \varepsilon' | f | i \rangle \langle i | f^{-1} \Sigma_E f^{-1} | j \rangle \langle j | f | \varepsilon \rangle, \quad (19)$$

with the “weighted” self-energy matrix $\langle i | f^{-1} \Sigma_E f^{-1} | j \rangle$, being calculated rather than $\langle i | \Sigma_E | j \rangle$.

B. Finite box size

In general, the finite box size may affect the results at low positron momenta $kR \lesssim 1$. In particular, it limits the range of the polarisation potential (represented by Σ_E) to distances not exceeding R . This is countered by adding a correction term to the self energy. At large distances the self-energy is local, energy independent and of the form $-\alpha_d/2r^4$, where α_d is the static dipole polarisability. The contribution to the self-energy matrix $\langle \varepsilon' | \Sigma_E | \varepsilon \rangle$ from distances outside the box can then be approximated by

$$\int_R^\infty P_{\varepsilon'\ell}(r) \left(-\frac{\alpha_d}{2r^4} \right) P_{\varepsilon\ell}(r) dr, \quad (20)$$

with the radial wavefunctions given by their asymptotic form,

$$P_{\varepsilon\ell}(r) = r \sqrt{\frac{k}{\pi}} \left[j_\ell(kr) \cos \delta_\ell^{(0)} - n_\ell(kr) \sin \delta_\ell^{(0)} \right], \quad (21)$$

in terms of the spherical Bessel and Neuman functions j_ℓ and n_ℓ , and the static HF field phaseshifts. The correction (20) is added to the self-energy matrix calculated using the many-body theory for $r \leq R$.

C. Angular momentum convergence

The use of B-spline basis sets provide for a fast convergence of the perturbation theory sums in the self-energy and Z_{eff} diagrams with respect to the number of intermediate electron and positron states in a given partial wave with angular momentum l . However, as numerical calculations are restricted to a finite number of partial waves up to a maximum orbital

angular momentum l_{\max} , the question of convergence with respect to l_{\max} also needs to be addressed. One solution successfully tested in Ref. [17] is to use extrapolation described by the asymptotic formulae [49],

$$\delta_\ell(k) = \delta_\ell^{[l_{\max}]}(k) + \frac{A_\ell(k)}{(l_{\max} + 1/2)^3}, \quad (22)$$

$$Z_{\text{eff}}(k) = Z_{\text{eff}}^{[l_{\max}]}(k) + \frac{B_\ell(k)}{(l_{\max} + 1/2)}, \quad (23)$$

where $\delta_\ell^{[l_{\max}]}(k)$ and $Z_{\text{eff}}^{[l_{\max}]}(k)$ are the phaseshift and annihilation parameter obtained for a given l_{\max} , and $A_\ell(k)$ and $B_\ell(k)$ are constants specific to a particular collision target, positron partial wave ℓ and momentum k . These constants and the extrapolated values of the phase shift and Z_{eff} are determined numerically by considering several data for points for a range of l_{\max} .

The use of Eqs. (22) and (23) to extrapolate phase shifts and Z_{eff} values to $l_{\max} \rightarrow \infty$ is illustrated in Fig. 6 for xenon. It shows that the numerical calculations adhere closely to the asymptotic form for $l_{\max} = 7-10$, allowing a reliable extrapolation to be made. This also indicates that although the extrapolation formulae are derived using perturbation theory [49], their use is also valid for the non-perturbative calculations presented here. Note that extrapolation is particularly important for Z_{eff} , where it contributes up to 30%, because the annihilation probability is sensitive to small electron-positron separations near the point of coalescence.

D. Partial-wave convergence of elastic scattering cross sections

The elastic scattering cross section is obtained as a sum over the partial waves [51],

$$\sigma_{\text{el}} = \frac{4\pi}{k^2} \sum_{\ell=0}^{\infty} (2\ell + 1) \sin^2 \delta_\ell. \quad (24)$$

At low positron energies only a few partial waves contribute to σ_{el} , and the contributions decrease quickly with ℓ . On the other hand, the contribution of higher partial waves is more important in the differential elastic cross section,

$$\frac{d\sigma_{\text{el}}}{d\Omega} = |f(\theta)|^2, \quad (25)$$

where

$$f(\theta) = \frac{1}{2ik} \sum_{\ell=0}^{\infty} (2\ell + 1) (e^{2i\delta_\ell} - 1) P_\ell(\cos \theta), \quad (26)$$

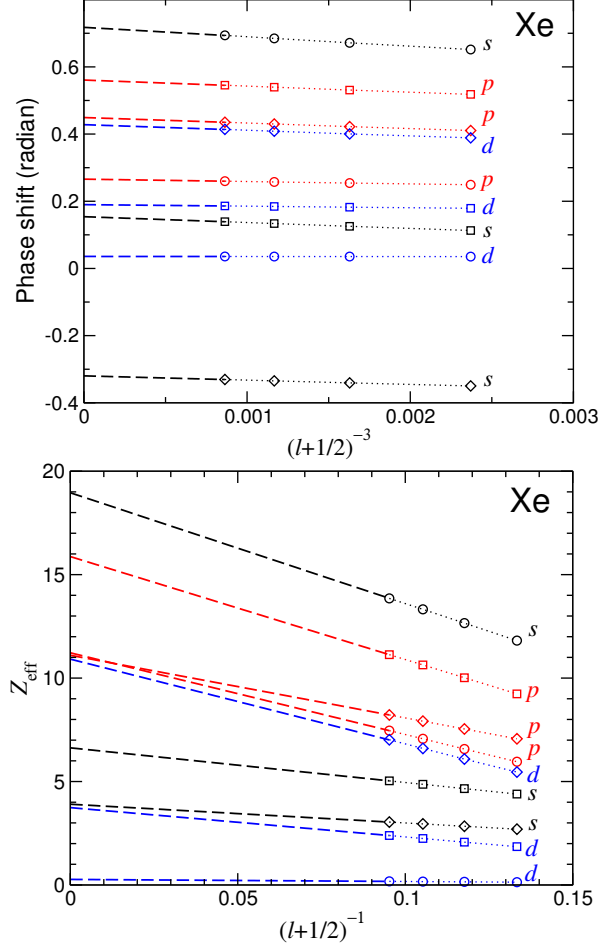


FIG. 6. Extrapolation of phase shifts and Z_{eff} for xenon with s -, p and d -wave incident positrons (black, red and blue symbols, respectively) of momenta: $k = 0.2$ a.u. (circles); $k = 0.4$ a.u. (squares); and $k = 0.6$ a.u. (diamonds). Dotted lines are shown as a guide only, dashed lines show extrapolation

is the scattering amplitude and $P_\ell(\cos \theta)$ are Legendre polynomials. Here large ℓ interfere constructively at small scattering angles θ and produce a characteristic cusp at $\theta = 0$.

As only s -, p - and d -wave phaseshifts have been calculated in the present work, some way must be found of accounting for the higher partial waves. This is done by noting that for higher partial waves, the dipole term in $\Sigma_E^{(2)} + \Sigma_E^{(3)}$ dominates the self-energy at low energies. At large distances it corresponds to the local energy-independent polarization potential $-\alpha_d/2r^4$. It alters the low-energy effective range expansion of the scattering phase

shifts [50],

$$\tan \delta_0 \simeq -ak \left[1 - \frac{\pi\alpha_d k}{3a} - \frac{4\alpha_d k^2}{3} \ln \left(C \frac{\sqrt{\alpha_d k}}{4} \right) \right]^{-1}, \quad (27)$$

$$\delta_\ell \simeq \frac{\pi\alpha_d k^2}{(2\ell - 1)(2\ell + 1)(2\ell + 3)}, \quad (\ell \geq 1), \quad (28)$$

where a is the scattering length and C is a positive constant. We use Eq. (27) to extract the scattering length from the s -wave numerical phaseshifts (see Sec. IV B), while Eq. (28) is applied for $\ell \geq 3$ in the calculation of elastic differential and total cross sections.

IV. RESULTS

A. Phase Shifts

Elastic scattering phase shifts are tabulated for the noble gas sequence in appendix B. The general features of the phase shift results are illustrated for krypton in Fig. 7. In the HF static field approximation, the phase shifts are negative, indicating a repulsive static field as is expected for positrons. Addition of the second-order correlation potential $\Sigma^{(2)}$ leads to an attractive positron-atom potential with a positive phase shift for low k . The asymptotic form of $\Sigma^{(2)}$ ($-\alpha_d/2r^4$) leads to terms quadratic in k in the low energy expansion of Eq. (27). As a result, the phase shifts reach a maximum and then fall off with increasing k , passing through zero to negative phase shifts at higher k . The higher-order contributions to the correlation potential have opposing effects. Inclusion of third-order screening diagrams $\Sigma^{(3)}$ decreases the strength of the positron-atom potential and therefore reduces the phase shifts whereas the contribution of virtual positronium formation, $\Sigma^{(\Gamma)}$ acts to increase the positron-atom potential. Virtual positronium formation makes an increasingly large contribution to the positron-atom potential as k increases. Comparison with the polarised orbital calculations of McEachran *et al.* [52] show good agreement for the s -wave phase shift with differences in the p and d -wave phase shifts for higher k . This can be attributed to the omission of virtual positronium formation in the polarised orbital method, with this omission being partially compensated for by an over-estimation of the second-order potential $\Sigma^{(2)}$ [2].

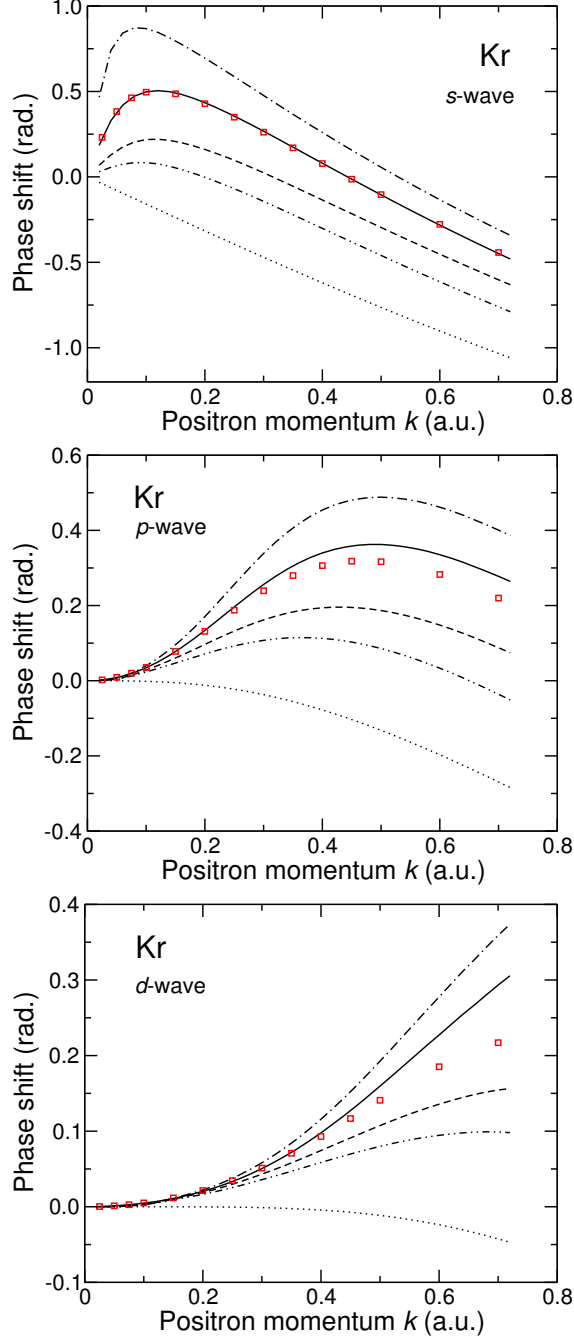


FIG. 7. Scattering phase shifts for s -, p - and d -wave positrons on Kr in various approximations to the positron wavefunction (see Figs. 1 and 3): HF static-field approximation (dotted curve); HF plus second-order correlation potential $\Sigma^{(2)}$ (dashed curve); HF + $\Sigma^{(2)}$ + $\Sigma^{(3)}$ (chain curve); HF + $\Sigma^{(2)}$ + $\Sigma^{(\Gamma)}$ (dot-dashed curve); and total: HF + $\Sigma^{(2)}$ + $\Sigma^{(3)}$ + $\Sigma^{(\Gamma)}$ (solid curve). Squares are theoretical results calculated using the polarised orbital method [52].

B. Scattering length

To characterise the strength of the positron-atom interaction at very low energies, it is useful to calculate the scattering length a which can be extracted from the s -wave phase shift δ_0 by expanding Eq. (27) (setting $C = 1$),

$$\tan \delta_0 = -ak - \frac{\pi\alpha_d k^2}{3} - \frac{4a\alpha_d}{3} k^3 \ln \frac{\sqrt{\alpha_d} k}{4} + Dk^3, \quad (29)$$

where D is a constant. For helium, neon, argon and krypton, one-point fits were made at $k = 0.02$. Due to the sensitivity for xenon of the scattering length to the scattering potential, both a one-point fit at $k = 0.02$ and a two-point fit at $k = 0.02, k = 0.04$ was examined as shown in Fig. 8. The one-point fit gave $a = -79.95$, with the two-point fit resulting in $a = -80.71, D = -180425$. Inclusion of terms of $\mathcal{O}(k^4)$ does not lead to an improved description of the present many-body phase shifts above $k = 0.04$ with the one-point fit in closer agreement. Here a value of $a \approx 80$ will be taken as our best estimate for the scattering length of xenon.

If the scattering length is large and negative then a virtual state exists at the energy $\epsilon = \hbar^2/2ma^2$ [51]. Table I compares scattering lengths extracted from the s -wave phase shifts with other theoretical and experimental results. Helium and neon display very close scattering lengths in the present calculations with the result for neon in good agreement with previous many-body theory calculations [23], although somewhat lower than other theoretical calculations [52], [53], [40]. For argon and krypton, there is close accord between the present many-body theory, polarized orbital [52], CCC calculations [40] and the experimental results of Zecca *et al.* [34, 35]. The scattering length increases across the sequence, giving rise to a virtual s -wave level for xenon of approximately 0.002 eV. This indicates that scattering calculations for xenon will display a high sensitivity to the representation of the polarisation potential in the low energy region. The many-body theory scattering length calculated here for xenon is in close to that calculated using polarised orbital theory [52], but a factor of 2 lower than that calculated from CCC theory [40] and from earlier many-body calculations [23] with the experimental result of [36] determined from extrapolating the low energy cross section with the aid of CCC calculations also a factor of 2 higher.

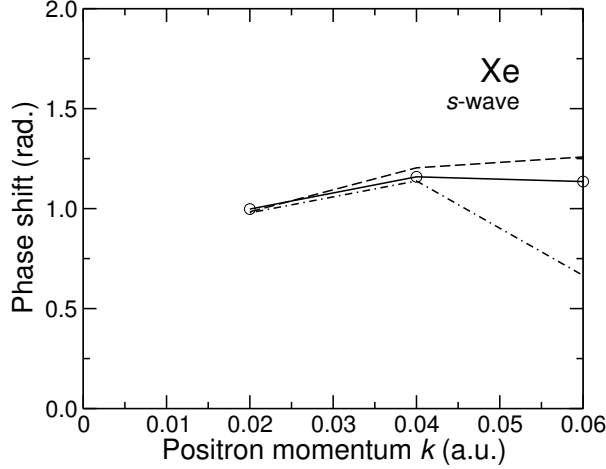


FIG. 8. s -wave elastic scattering phase shift for Xe. Solid, present many-body theory; dashed, one-point fit of Eq. (29) at $k = 0.02$; dot-dashed, two-point fit of Eq. (29) at $k = 0.02$ and $k = 0.04$.

TABLE I. Scattering lengths, a , in a.u. for the noble gases.

Atom	He	Ne	Ar	Kr	Xe
$a^{[1]}$	-0.43	-0.45	-4.4	-9.7	-80.0
$a^{[2]}$		-0.43	-3.9	-9.1	≈ 100
$a^{[3]}$	-0.53	-0.61	-5.3	-10.4	-45
$a^{[4]}$	-0.48				
$a^{[5]}$		0.53	-4.3	-11.2	-117
$a^{[6]}$			-4.9 ± 0.7	-10.3 ± 1.5	-99.2 ± 18.4

[1] Present many-body calculations;

[2] Previous many-body calculations [23];

[3] Polarized orbital calculations [52];

[4] Kohn variational calculations [53];

[5] Convergent close-coupling calculations [40];

[6] Experiment: Ar [35], Kr [34], Xe [36].

C. Elastic scattering cross section

The elastic scattering cross sections along the noble gas sequence are shown in figures 9-13 in comparison with existing experimental and theoretical data. The numerical cross sections are tabulated in appendix B.

For helium, our many-body theory calculations agree closely with the variational calculations of [54], the convergent close-coupling results of [55] and the experimental measurements of Refs. [56], [57], and [33]. A consensus on the elastic scattering cross section appears to have been reached. The polarised orbital results of [52] are not in agreement with other theoretical and experimental data, and the magnetic-field-free experimental measurements of Nagumo *et al.* are larger than all theory and experimental results.

For Neon, examining theoretical data, the many-body theory results agree most closely with the relativistic polarised orbital results of [38]. At energies below 2 eV, the present many-body theory results agree well with the previous many-body theory calculations of [23] at energies below 2 eV, but trend lower above this energy. The convergent close-coupling results of [40] are higher than the other calculations and the polarised orbital results of [52] are considerably lower than both experiment and theory at energies above 2 eV. Moving to a comparison with experimental data, the present many-body theory results agree most closely with the recent measurements of Sullivan *et al.* [37] above 2 eV, but are lower than Sullivan's results below this energy where they agree better with the measurements of Stein *et al.* [56]

For argon, the many-body theory results agree well with the convergent close-coupling results of [40], but are higher than the non-relativistic and relativistic polarised orbital results [39, 52] above 2 eV. Comparing to experiment, the many-body theory results are in good agreement with the measurements of Sinapius *et al.* [59], Zecca *et al.* [35] and Sullivan *et al.* [37].

For krypton, the convergent close-coupling results of [40] are in good agreement with the many-body theory results, with the polarised orbital results [38] [CHECK] [52] lower than other theoretical results above 1 eV. The experimental data of Sinapius *et al.* [59], Zecca *et al.* [34] and Sullivan *et al.* [38] are in good agreement with each-other and the many-body theory results. The measurements of Dababneh *et al.* [62] and Coleman *et al.* [58] lie below the many-body theory results.

For xenon, the present many-body theory results are in excellent agreement with the convergent close-coupling results of [40], lower than previous many-body theory calculations of [23] and somewhat higher than the non-relativistic and relativistic variants of the polarised orbital method [39, 52]. Compared to experiment the present results agree most closely with the measurements of Sinapius *et al.* [59] and Sullivan *et al.* The experimental results of Dababneh *et al.* [62] and Coleman *et al.* [58] lie below the other experimental results and the present many-body theory calculations. A possible reason for this may lie in the fact that the differential scattering cross section for positron scattering on heavier noble gases is strongly forward peaked. Poor detection of forward-scattered positrons [60] will cause an underestimate in the cross section.

Some general trends can be seen in the elastic scattering cross sections across the noble gas sequence. The many-body theory results are in good agreement with non-perturbative convergent close-coupling results [40], apart from neon where there is a discrepancy that will need further investigation. The polarised orbital results [52] are seen to underestimate the cross sections at higher energies due to the neglect of virtual positronium formation. Agreement with recent experimental measurements [33–39] is generally close.

D. Differential cross sections

A more sensitive test of the accuracy of a scattering calculation is the differential cross section,

$$\frac{d\sigma}{d\Omega} = |f(\theta)|^2, \quad (30)$$

where the scattering amplitude $f(\theta)$ is given by,

$$f(\theta) = \sum_{\ell=0}^{\infty} (2\ell + 1) \frac{e^{2i\delta_{\ell}} - 1}{2ik} P_{\ell}(\cos \theta). \quad (31)$$

By making use of Eq. (28) for higher partial waves, Eq. (31) may be written as,

$$f(\theta) = \sum_{\ell=0}^{\ell_0} (2\ell + 1) \left[\frac{e^{2i\delta_{\ell}} - 1}{2ik} - \frac{\pi\alpha_d k^2}{(2\ell - 1)(2\ell + 1)(2\ell + 3)} \right] \times P_{\ell}(\cos \theta) - \frac{\pi\alpha_d k}{2} \sin \frac{\theta}{2}, \quad (32)$$

where ℓ_0 is the maximum partial wave for which the phase shift has been calculated.

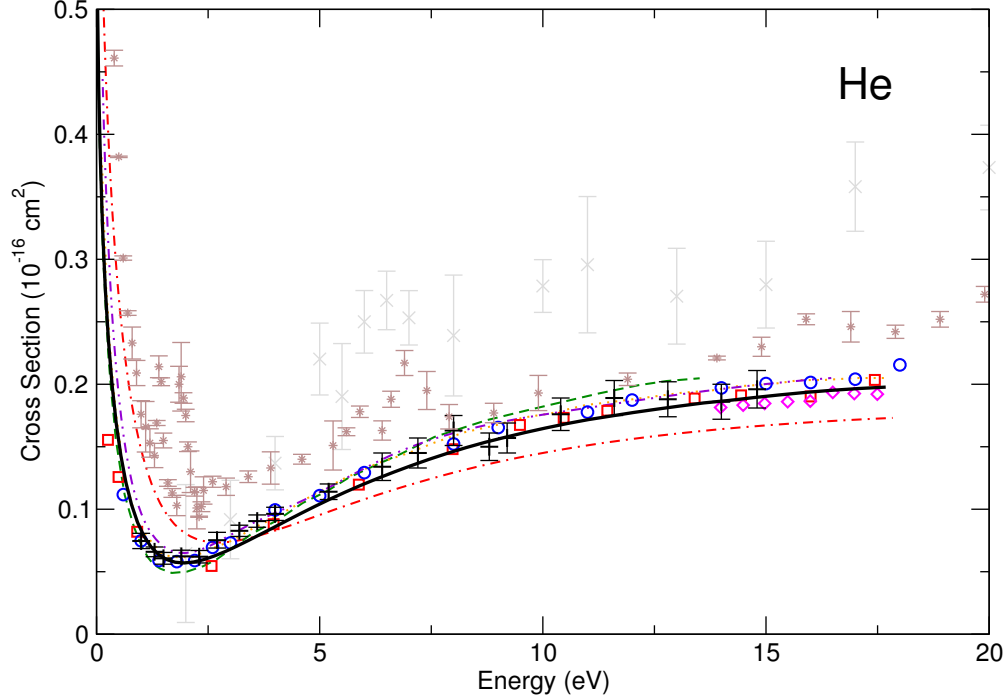


FIG. 9. Elastic scattering cross section for He. Theory: solid, present many-body theory; dot-dashed, polarized orbital, [52]; dashed, MBPT [23]; dotted, CCC [55]; dot-dot-dashed, Kohn variational [54]; experiment: squares, Stein *et al.* [56]; circles, Mizogawa *et al.* [57]; stars, Karwasz *et al.* [75]; diamonds, Coleman *et al.* [58]; plus, Sullivan *et al.* [33]; crosses, Nagumo *et al.* [73].

Figures 14 and 15 compare differential cross sections calculated using our many-body phase shifts for krypton and xenon at an incident positron energy of 2eV with other theoretical calculations and experimental data from the Surko [63, 64] and Sullivan groups [38, 39]. It is important to note that the Surko and Sullivan groups use a positron trap to accumulate positrons, which can then be used to form a pulsed, energy tunable positron beam. This beam is magnetically guided to the target gas cell. However, the apparatus is not able to distinguish between forward scattered and back-scattered particles, as any back-scattered particles are reflected and passed back through the gas cell. The measured differential cross section for an angle θ is therefore the sum of the cross sections at an angle θ and $180 - \theta$. Theoretical results have therefore been folded about 90° where necessary.

For krypton, the present many-body theory calculations are in good agreement with CCC calculations [34], non-relativistic and relativistic variants of the polarised orbital method [38, 52], and the experimental results of [63] and [38] across the angular range, with the CCC

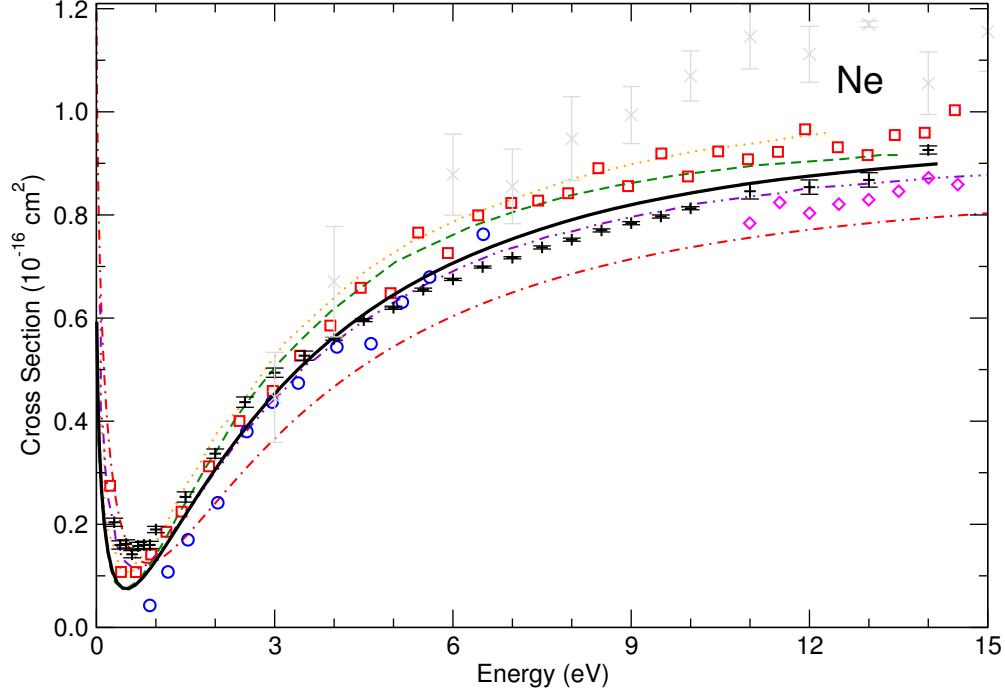


FIG. 10. Elastic scattering cross section for Ne. Theory: solid, present many-body theory; dot-dashed, polarized orbital, [52]; dashed, MBPT [23]; dotted, CCC [40]; dot-dot-dashed, relativistic polarised orbital [37]; experiment: squares, Stein *et al.* [56]; circles, Sinapius *et al.* [59]; diamonds, Coleman *et al.* [58]; plus, Sullivan *et al.* [37]; crosses, Nagumo *et al.* [74].

results trending slightly higher at small angles. However, a large discrepancy is observed with the polarisation calculations of [65]. In the case of xenon, there is excellent agreement between the present many-body calculations and the CCC calculations of [39], with both calculations somewhat higher than the relativistic polarised orbital calculations of [39]. As for krypton, the presents results show a large difference with the polarisation calculations of [65]. The many-body and CCC calculations are in better agreement with the experiment of [39] than that of [64], with both experiments in better agreement with each-other above 40° .

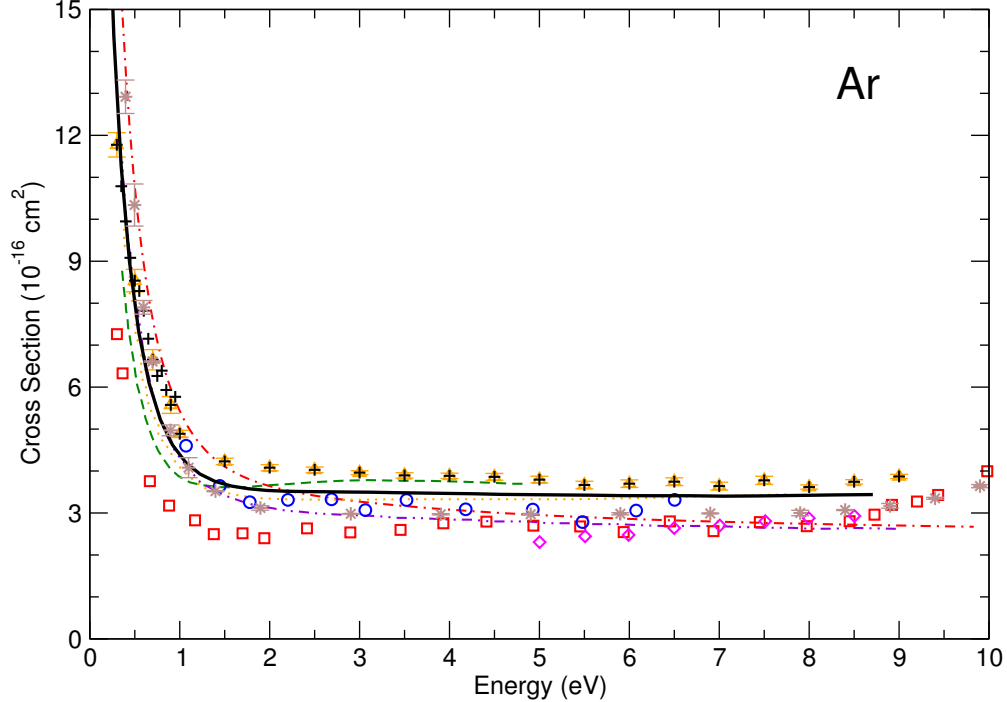


FIG. 11. Elastic scattering cross section for Ar. Theory: solid, present many-body theory; dot-dashed, polarized orbital, [52]; dashed, MBPT [23]; dotted, CCC [40]; dot-dot-dashed, relativistic polarised orbital [37]; experiment: squares, Stein *et al.* [61]; circles, Sinapius *et al.* [59]; stars, Karwasz *et al.* [76]; diamonds, Coleman *et al.* [58]; triangles, Zecca *et al.* [35]; plus, Sullivan *et al.* [37].

V. POSITRON ANNIHILATION

A. Energy resolved Z_{eff}

Partial-wave contributions to Z_{eff} are plotted in Fig. 16 for the noble gas sequence as a function of the positron momentum. As one moves along the noble gas sequence, the s -wave Z_{eff} becomes increasingly large and energy dependent, at low energies. This strong energy dependence is due to the existence of positron-atom virtual levels [24, 25] which is signified by large scattering lengths a . It is possible to derive an analytic form for the behaviour of Z_{eff} at small positron momenta when the positron-atom system supports a virtual state. It is clear from equation (14) that Z_{eff} is proportional to the positron density near the atom. For an s -wave positron with a small momentum k , its wavefunction just outside

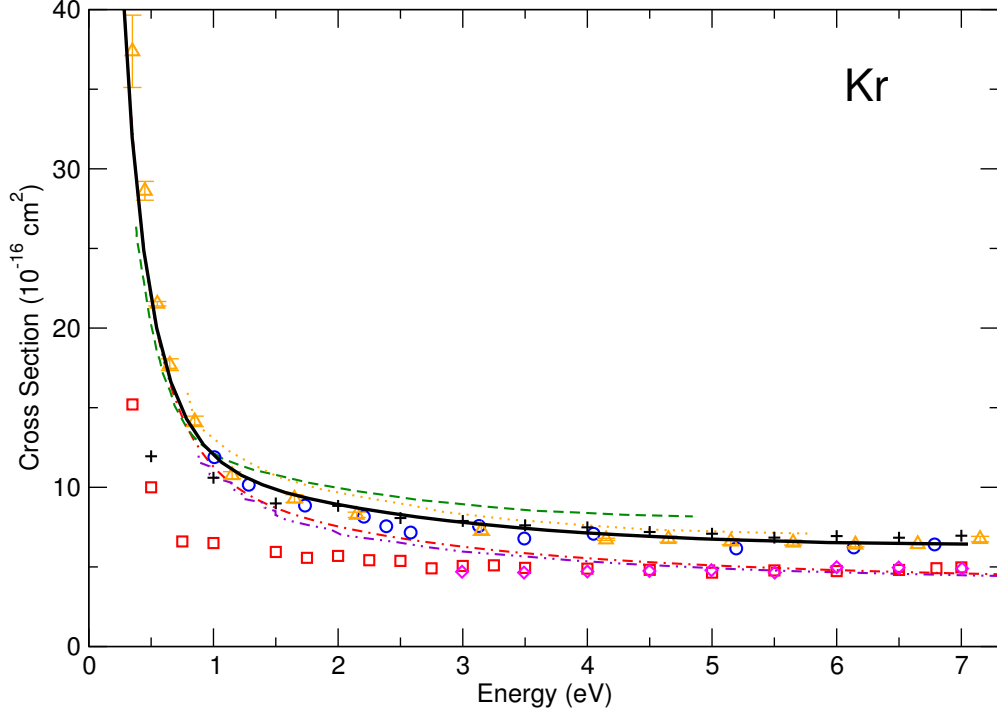


FIG. 12. Elastic scattering cross section for Kr. Theory: solid, present many-body theory; dot-dashed, polarized orbital, [52]; dashed, MBPT [23]; dotted, CCC [40]; dot-dot-dashed, relativistic polarised orbital [38]; experiment: squares, Dababneh *et al.* [62]; circles, Sinapius *et al.* [59]; diamonds, Coleman *et al.* [58]; triangles, Zecca *et al.* [34]; plus, Sullivan *et al.* [38].

the atom has the form $\psi = 1 + (f/r)$ where f is the scattering amplitude and $kr \ll 1$. If a virtual level exists for the positron the scattering amplitude can be approximated by the formula $f = -1/(\kappa + ik)$ [51], where $\kappa = 1/a$. The magnitude of the many-particle wavefunction of the positron-atom system in the region around the atomic radius r_a where the annihilation occurs is proportional to ψ , as the two wavefunctions must join smoothly at r_a . If the scattering length is large, $|a| \gg r_a$, then the f/r term will dominate the positron wavefunction and the momentum dependence of Z_{eff} will then be given by the formula,

$$Z_{\text{eff}}(k) = \frac{K}{\kappa^2 + k^2} + A. \quad (33)$$

where K and A are constants, with A accounting for higher partial wave contributions to Z_{eff} . It is clear that if the thermal positron momentum k is smaller than κ then the annihilation rate will be proportional to the scattering length squared.

The p -wave Z_{eff} also appears to show the formation of a broad shape resonance. This is

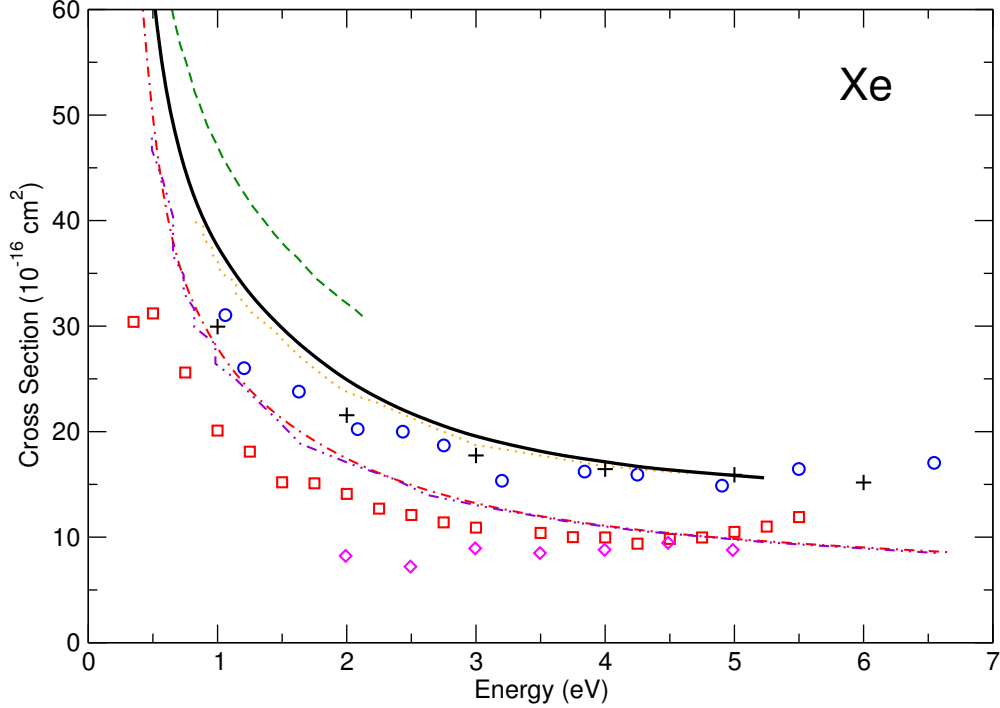


FIG. 13. Elastic scattering cross section for Xe. Theory: solid, many-body theory; dot-dashed, polarized orbital [52]; dashed, Gribakin *et al.* [23]; dotted, CCC [40]; dot-dot-dashed, relativistic polarised orbital [39]; experiment: squares, Dababneh *et al.* [62]; circles, Sinapius *et al.* [59]; plus, Sullivan *et al.* [39]; diamonds, Coleman *et al.* [58].

supported by the behaviour of the p -wave phase shift shown for krypton in Fig. 7.

B. Thermally averaged Z_{eff}

Most of the available experimental data for Z_{eff} has been obtained for thermalised positrons at room temperature. As can be seen in Fig. 16, apart from xenon, the noble gas atoms show a relatively weak energy dependence around the region of thermal positron momenta ($k \approx 0.045$ au). Therefore the value of Z_{eff} taken at $k \approx 0.044$ can serve as a thermal Z_{eff} for helium, neon, argon and krypton. However, the Z_{eff} of xenon is strongly energy dependent and so must be averaged over the Maxwellian distribution.

To obtain a thermally averaged Z_{eff} , \bar{Z}_{eff} , $Z_{\text{eff}}(k)$ as given by Eq. (33) is convolved with the Maxwellian distribution [23],

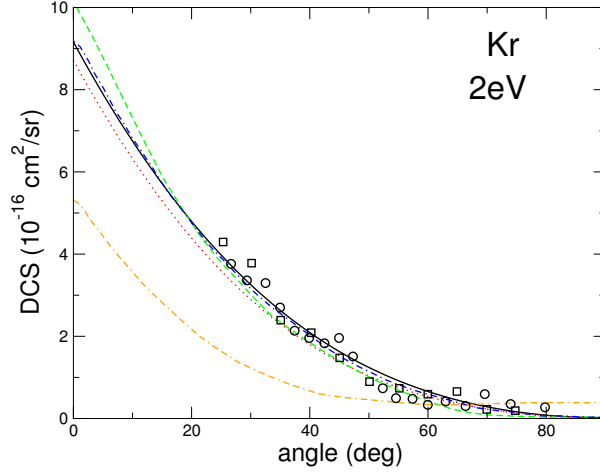


FIG. 14. Differential elastic scattering cross section for Kr. Theory: solid, present many-body theory; dotted, polarized orbital, [52]; dashed, CCC [34]; dot-dashed, relativistic polarised orbital [38]; dashed-dashed-dotted, polarisation potential [65]; experiment: circles, Gilbert *et al.* [63]; squares, Sullivan *et al.* [38].

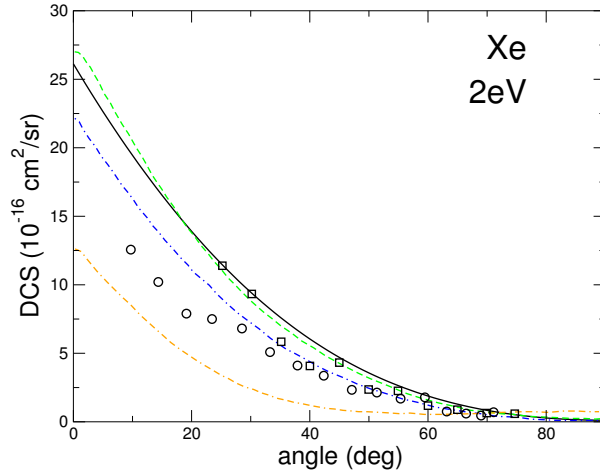


FIG. 15. Differential elastic scattering cross section for Xe. Theory: solid, present many-body theory; dashed, CCC [39]; dot-dashed, relativistic polarised orbital [39]; dashed-dashed-dotted, polarisation potential [65]; experiment: circles, Marler *et al.* [64]; squares, Sullivan *et al.* [39].

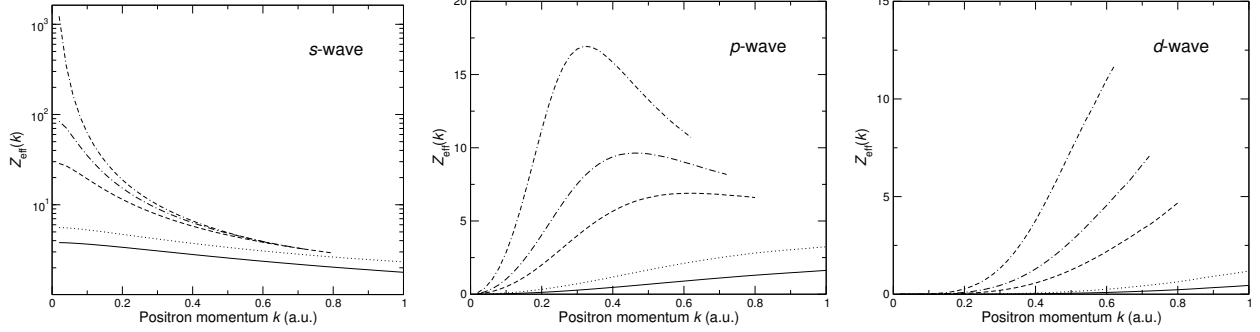


FIG. 16. Z_{eff} for s -, p - and d -wave positron annihilation on the valence subshells of the noble gases: helium (solid line); neon (dotted line); argon (dashed line); krypton (dash-dotted line) and xenon (dash-dash-dotted line).

$$\begin{aligned} \bar{Z}_{\text{eff}} &= A + \int_0^\infty Z_{\text{eff}}(k) \frac{\exp(-k^2/2k_B T)}{(2\pi k_B T)^{3/2}} 4\pi k^2 dk \\ &= A + \frac{K}{k_B T} \left\{ 1 - \sqrt{\frac{\pi \kappa^2}{2k_B T}} \exp(-k^2/2k_B T) \left[1 - \Phi \left(\sqrt{\frac{\pi \kappa^2}{2k_B T}} \right) \right] \right\}, \end{aligned} \quad (34)$$

where $\Phi(x) = \frac{2}{\sqrt{\pi}} \int_0^x \exp^{-t^2} dt$ and k_B the Boltzmann constant.

By fitting the sum of the energy resolved s -, p - and d -wave Z_{eff} for xenon to Eq. (33) using K , κ and A as free parameters, values of $K = 0.55$, $\kappa = 0.00067$ and $A = 19.62$ are obtained. The fit is shown in Fig. 17 with good agreement seen between the calculated and fitted Z_{eff} . However, it should be noted that the presence of the virtual s -level for xenon, which leads to a strong energy dependence of Z_{eff} in the region of thermal positron momenta, causes the fit using Eq. (33) to be highly sensitive to the accuracy of the calculated Z_{eff} at low k .

Substitution into Eq. (34) then gives an estimate of $\bar{Z}_{\text{eff}} = 440.2$. This compares to a simple sum of s -, p - and d -wave Z_{eff} at $k = 0.044$ of 325.48, illustrating the importance in the case of xenon of the thermal averaging.

Values of \bar{Z}_{eff} along the noble gas sequence are shown in table II in comparison with available experimental data.

For helium the present many-body theory results are in good agreement with precise variational calculations for helium [66] and with the measurements of [6]. For neon, argon and krypton the many-body results are in close agreement with the results of [6], but differ

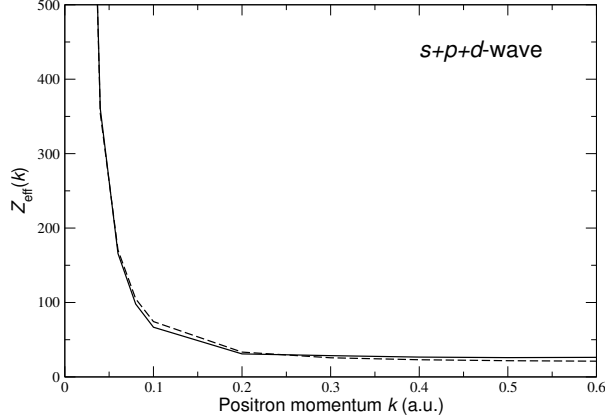


FIG. 17. Sum of xenon s -, p - and d -wave $Z_{\text{eff}}(k)$. Solid, present many-body theory; dashed, fit to many-body results using Eq. (33).

TABLE II. Thermally averaged Z_{eff} for the noble gases.

Atom	He	Ne	Ar	Kr	Xe
$\bar{Z}_{\text{eff}}^{[1]}$	3.79	5.56	26.75	69.66	440.2
$\bar{Z}_{\text{eff}}^{[2]}$	3.88	6.98	30.5	56.3	202
$\bar{Z}_{\text{eff}}^{[2]}$	3.94	5.99	26.77	65.7	320, 400-450
$\bar{Z}_{\text{eff}}^{[3]}$	–	–	33.8	90.1	401

[1] Present many-body theory calculations.

[2] He: Kohn variational calculations [66];

Ne, Ar, Kr, Xe: polarised orbital calculations [52].

[3] Experiment: He, Ne, Ar [6]; Kr, Xe, [67].

[4] Experiment: Ar and Kr [68]; Xe [7].

significantly from the experimental results for argon and krypton of [68] and are lower than polarised orbital calculations [52]. Even assuming an error of 5-10% in the many-body calculations, the results of [68] appear to be anomalously high. For xenon, the many-body result is much higher than polarised orbital calculations [52] and is in reasonable accord with the experiment of [7].

To gain a better understanding of the discrepancies between theory and experiment, it is necessary to examine the experimental techniques used to measure \bar{Z}_{eff} . The results of

[6] were obtained using positron lifetime spectroscopy. In this technique the lifetime of a positron is determined by first detecting the nuclear gamma ray that is emitted in the β^+ decay of a radioactive isotope, e.g. ^{22}Na . The positron is then injected into a gas cell where it thermalises and annihilates. The two 511 keV gamma rays arising from positron annihilation are detected in coincidence. The difference in times between these two events gives the lifetime of a positron. By measuring the lifetime of $10^6 - 10^7$ positrons it is possible to obtain a lifetime spectrum. The annihilation rate can then be found from the gradient of this spectrum. The results of [68] and [7] were obtained using a positron trap. A low energy positron beam is introduced into a Penning trap that is able to confine the positrons in the presence of a buffer gas, such as N_2 . The positrons lose energy through electronic excitation of the gas and cool to thermal energies by vibrational and rotational excitation of the gas. Differential pumping of the buffer gas allows the thermal positrons to be stored in a high vacuum region of the trap. A test gas is then injected into the trap, and the positron annihilation rate is found by determining the number of positrons remaining as a function of time.

For argon and krypton the discrepancy between the results of [68] and [6] is concerning. Positron lifetime measurements of \bar{Z}_{eff} have been repeated for Argon and Krypton [67]. Excellent agreement was found with the results of [6]. Thermalisation should not be an important problem for argon and krypton, and Z_{eff} is not as strongly energy dependent. The better agreement of the many-body results with those of [6] leaves the positron trap results for argon and krypton suspect. It would be worthwhile for new positron trap measurements of \bar{Z}_{eff} for argon and krypton to be performed to help resolve this discrepancy.

For xenon, positron lifetime measurements have been performed for a pure xenon gas [67] that replicated a result of $\bar{Z}_{\text{eff}} \approx 320$ consistent with earlier measurements [6]. However, when a small amount of a gas such as H_2 , was added, \bar{Z}_{eff} increased to 400–450 [67], in good agreement with the present many-body calculations. These results indicate that incomplete thermalisation of the positrons can be a major issue in experimental determinations of \bar{Z}_{eff} for xenon. Thermalisation of positrons in an atomic gas is achieved through elastic collisions. Thermalisation of positrons in a heavy atom gas, such as xenon, will therefore be very slow. The large values and strong energy dependence of Z_{eff} for xenon has the effect that many positrons will annihilate before thermalisation. Another problem with experiments for xenon is that the large scattering length implies that very low gas pressures must be used in order

to avoid clustering or multiple scattering effects, i.e., the inter-atomic distance should be greater than the scattering length. The positron trap technique which uses very low gas pressures is able to circumvent these problems, and so the results of [7] are expected to be more reliable. The current calculations and available experimental data indicates that the value of \bar{Z}_{eff} for xenon lies in the range 400–450.

VI. CONCLUSIONS

The many-body formalism that has been developed to study positron scattering and annihilation from atoms and ions [17, 27, 29] has been applied to the noble gas sequence. Good agreement with experimental data and recent non-perturbative CCC calculations has been obtained for the elastic scattering cross sections. Calculation of the thermally averaged Z_{eff} should help to guide future experiments. The large value of \bar{Z}_{eff} for xenon has been shown to arise from the presence of a positron-xenon virtual level.

Through this work, together with Ref. [9], the many-body theory method has provided a near complete understanding of the positron-noble gas atom system at positron energies below Ps-formation threshold. Positron-scattering phase shifts and cross sections, and rates and γ -spectra for positron annihilation on core and valence electrons, have been calculated in a consistent framework that takes proper account of positron-atom and positron-electron correlations.

There are, however, a number of ways in which the many-body theory can be developed and applied. In future, we hope to extend our many-body theory to a fully relativistic formalism. This will be important in exploring the influence that relativistic effects have on positron scattering from high Z atoms and ions, particularly for positron annihilation on inner shells. It will also be important to account for higher-order polarisation effects [69, 70] beyond the third order many-body diagrams included in the present work, particularly for xenon where the low-energy cross section is highly sensitive to polarisation effects. Another area of interest is the application of the many-body theory to open-shell systems. Although only trully rigorous for closed shell systems, approximate methods can be introduced that should allow a reasonably accurate application of the theory to such systems. This would be particularly useful for studies of positron annihilation on core electrons in condensed matter systems [9, 71].

ACKNOWLEDGMENTS

DGG is grateful to the Institute for Theoretical Atomic, Molecular and Optical Physics, at the Harvard-Smithsonian Centre for Astrophysics (Cambridge, MA, USA), where he carried out part of this work as a visitor, and is indebted to H. R. Sadeghpour and colleagues for their generous hospitality. DGG was supported by DEL Northern Ireland.

Appendix A: Algebraic form of the many-body diagrams

The algebraic expressions for the various many-body diagrams are tabulated below and complement those provided in Appendix A of Ref. [17]. The derivation of these expressions makes extensive use of graphical techniques for performing angular momentum algebra [72].

Let us denote the direct reduced Coulomb matrix element by

$$\begin{aligned} \langle 3, 4 || V_l || 2, 1 \rangle &= \sqrt{[l_3][l_4][l_2][l_1]} \begin{pmatrix} l_1 & l & l_3 \\ 0 & 0 & 0 \end{pmatrix} \begin{pmatrix} l_2 & l & l_4 \\ 0 & 0 & 0 \end{pmatrix} \\ &\times \iint P_{\varepsilon_3 l_3}(r_1) P_{\varepsilon_4 l_4}(r_2) \frac{r^l}{r^{l+1}} P_{\varepsilon_2 l_2}(r_2) P_{\varepsilon_1 l_1}(r_1) dr_1 dr_2, \end{aligned} \quad (\text{A1})$$

where $[l] \equiv 2l + 1$. Secondly, we denote the reduced Coulomb matrix element for an electron-positron pair with the total angular momentum J by

$$\langle 3, 4 || V^{(J)} || 1, 2 \rangle = \sum_l (-1)^{J+l} \left\{ \begin{matrix} J & l_3 & l_4 \\ l & l_2 & l_1 \end{matrix} \right\} \langle 3, 4 || V_l || 2, 1 \rangle. \quad (\text{A2})$$

Note that this is similar to the ‘exchange’ matrix elements that one meets in electron scattering [12, 13, 43]. These matrix elements form the main components of the analytic expressions represented by the diagrams. The additional rules are as follows. For closed-shell atoms, each electron-hole ‘loop’ gives a spin factor of 2. In addition, asymmetric Z_{eff} diagrams should contain an extra factor of 2 arising from their mirror images. The sign of each diagram is given by $(-1)^{a+b+c}$, where a is the number of hole lines, b is the number of ‘loops’ and c is the number of positron-electron interactions.

Matrix elements of the δ -function operator are defined similarly to those of the Coulomb interaction. We denote the direct matrix element by

$$\begin{aligned} \langle 3, 4 || \delta_l || 2, 1 \rangle &= \frac{[l]}{4\pi} \sqrt{[l_3][l_4][l_2][l_1]} \begin{pmatrix} l_1 & l & l_3 \\ 0 & 0 & 0 \end{pmatrix} \begin{pmatrix} l_2 & l & l_4 \\ 0 & 0 & 0 \end{pmatrix} \\ &\times \int P_{\varepsilon_3 l_3}(r) P_{\varepsilon_4 l_4}(r) \frac{1}{r^2} P_{\varepsilon_2 l_2}(r) P_{\varepsilon_1 l_1}(r) dr, \end{aligned} \quad (\text{A3})$$

and the matrix element for a positron-electron pair coupled to an angular momentum J by

$$\langle 3, 4 \| \delta^{(J)} \| 1, 2 \rangle = \sum_l (-1)^{J+l} \begin{Bmatrix} J & l_3 & l_4 \\ l & l_2 & l_1 \end{Bmatrix} \langle 3, 4 \| \delta^{(J)} \| 2, 1 \rangle. \quad (\text{A4})$$

The algebraic expressions for the third-order contributions to $\langle \varepsilon' | \Sigma_E | \varepsilon \rangle$ shown by the diagrams in Fig. 3(a)–(e) are, respectively:

$$- \sum_{\substack{\nu, \mu_1, \mu_2 > F \\ n_1, n_2 \leq F}} \sum_l \frac{2 \langle \varepsilon', n_2 \| V_l \| \mu_2, \nu \rangle \langle \mu_2, n_1 \| V^{(l)} \| \mu_1, n_2 \rangle \langle \nu, \mu_1 \| V_l \| n_1, \varepsilon \rangle}{(2l+1)(2l+1)(E + \varepsilon_{n_2} - \varepsilon_\nu - \varepsilon_{\mu_2})(E + \varepsilon_{n_1} - \varepsilon_\nu - \varepsilon_{\mu_1})}, \quad (\text{A5})$$

$$\sum_{\substack{\nu, \mu_1, \mu_2 > F \\ n_1, n_2 \leq F}} \sum_l \frac{4 \langle \varepsilon', n_2 \| V_l \| \mu_2, \nu \rangle \langle n_1, \mu_2 \| V_l \| n_2, \mu_1 \rangle \langle \nu, \mu_1 \| V_l \| n_1, \varepsilon \rangle}{(2l+1)^2(2l+1)(E + \varepsilon_{n_2} - \varepsilon_\nu - \varepsilon_{\mu_2})(E + \varepsilon_{n_1} - \varepsilon_\nu - \varepsilon_{\mu_1})}, \quad (\text{A6})$$

$$\sum_{\substack{\nu, \mu_1, \mu_2 > F \\ n_1, n_2 \leq F}} \sum_l \frac{4 \langle \varepsilon', n_2 \| V_l \| \mu_2, \nu \rangle \langle \mu_1, \mu_2 \| V_l \| n_2, n_1 \rangle \langle \nu, n_1 \| V_l \| \mu_1, \varepsilon \rangle}{(2l+1)^2(2l+1)(E + \varepsilon_{n_2} - \varepsilon_\nu - \varepsilon_{\mu_2})(\varepsilon_{n_1} + \varepsilon_{n_2} - \varepsilon_{\mu_1} - \varepsilon_{\mu_2})}, \quad (\text{A7})$$

$$- \sum_{\substack{\nu, \mu_1, \mu_2 > F \\ n_1, n_2 \leq F}} \sum_l \frac{2 \langle \varepsilon', n_2 \| V_l \| \mu_1, \nu \rangle \langle \mu_1, \mu_2 \| V^{(l)} \| n_1, n_2 \rangle \langle \nu, n_1 \| V_l \| \mu_2, \varepsilon \rangle}{(2l+1)(2l+1)(E + \varepsilon_{n_2} - \varepsilon_\nu - \varepsilon_{\mu_1})(\varepsilon_{n_1} + \varepsilon_{n_2} - \varepsilon_{\mu_1} - \varepsilon_{\mu_2})}, \quad (\text{A8})$$

$$\sum_{\substack{\nu_1, \nu_2, \mu > F \\ n_1, n_2 \leq F}} \sum_{l, l', l''} (-1)^{l+l+l_{n_1}} \frac{2 \langle \varepsilon', n_2 \| V_{l''} \| \mu, \nu_2 \rangle \langle \nu_2, n_1 \| V_{l'} \| n_2, \nu_1 \rangle \langle \nu_1, \mu \| V_l \| n_1, \varepsilon \rangle}{(2l+1)(E + \varepsilon_{n_2} - \varepsilon_{\nu_2} - \varepsilon_\mu)(E + \varepsilon_{n_1} - \varepsilon_{\nu_1} - \varepsilon_\mu)} \begin{Bmatrix} l_{\nu_1} & l' & l_{\nu_2} \\ l'' & \ell & l \end{Bmatrix} \begin{Bmatrix} l & l' & l'' \\ l_{n_2} & l_\mu & l_{n_1} \end{Bmatrix} \quad (\text{A9})$$

where ℓ is the orbital angular momentum of the incident positron, “ $> F$ ” indicates summation over the excited electron states (i.e., those above the Fermi level), and “ $\leq F$ ” indicates summation over the hole states (i.e., those at or below the Fermi level).

Similarly, the algebraic expressions for the Z_{eff} diagrams in Fig. 5(a)–(g), are, respectively:

$$2 \sum_{\substack{\nu, \mu_1, \mu_2 > F \\ n_1, n_2 \leq F}} \sum_l \frac{2 \langle \varepsilon, n_2 \| \delta_l \| \mu_2, \nu \rangle \langle \mu_2, n_1 \| V^{(l)} \| \mu_1, n_2 \rangle \langle \nu, \mu_1 \| V_l \| n_1, \varepsilon \rangle}{(2l+1)(2l+1)(E + \varepsilon_{n_2} - \varepsilon_\nu - \varepsilon_{\mu_2})(E + \varepsilon_{n_1} - \varepsilon_\nu - \varepsilon_{\mu_1})}, \quad (\text{A10})$$

$$-2 \sum_{\substack{\nu_1, \nu_2, \mu > F \\ n_1, n_2 \leq F}} \sum_{l, l', l''} (-1)^{l+l+l_{n_1}} \frac{2 \langle \varepsilon, n_2 \| \delta_{l''} \| \mu, \nu_2 \rangle \langle \nu_2, n_1 \| V_{l'} \| n_2, \nu_1 \rangle \langle \nu_1, \mu \| V_l \| n_1, \varepsilon \rangle}{(2l+1)(E + \varepsilon_{n_2} - \varepsilon_{\nu_2} - \varepsilon_\mu)(E + \varepsilon_{n_1} - \varepsilon_{\nu_1} - \varepsilon_\mu)} \begin{Bmatrix} l_{\nu_1} & l' & l_{\nu_2} \\ l'' & \ell & l \end{Bmatrix} \begin{Bmatrix} l & l' & l'' \\ l_{n_2} & l_\mu & l_{n_1} \end{Bmatrix} \quad (\text{A11})$$

$$-2 \sum_{\substack{\nu, \mu_1, \mu_2 > F \\ n_1, n_2 \leq F}} \sum_l \frac{4 \langle \varepsilon, n_2 \| \delta_l \| \mu_2, \nu \rangle \langle n_1, \mu_2 \| V_l \| n_2, \mu_1 \rangle \langle \nu, \mu_1 \| V_l \| n_1, \varepsilon \rangle}{(2l+1)^2(2l+1)(E + \varepsilon_{n_2} - \varepsilon_\nu - \varepsilon_{\mu_2})(E + \varepsilon_{n_1} - \varepsilon_\nu - \varepsilon_{\mu_1})}, \quad (\text{A12})$$

$$-2 \sum_{\substack{\nu, \mu_1, \mu_2 > F \\ n_1, n_2 \leq F}} \sum_l \frac{4 \langle \varepsilon, n_2 | \delta_l | \mu_2, \nu \rangle \langle \mu_1, \mu_2 | V_l | n_2, n_1 \rangle \langle \nu, n_1 | V_l | \mu_1, \varepsilon \rangle}{(2l+1)^2 (2l+1) (E + \varepsilon_{n_2} - \varepsilon_\nu - \varepsilon_{\mu_2}) (\varepsilon_{n_1} + \varepsilon_{n_2} - \varepsilon_{\mu_1} - \varepsilon_{\mu_2})}, \quad (\text{A13})$$

$$-2 \sum_{\substack{\nu, \mu_1, \mu_2 > F \\ n_1, n_2 \leq F}} \sum_l \frac{4 \langle \varepsilon, n_2 | V_l | \mu_2, \nu \rangle \langle \mu_1, \mu_2 | V_l | n_2, n_1 \rangle \langle \nu, n_1 | \delta_l | \mu_1, \varepsilon \rangle}{(2l+1)^2 (2l+1) (E + \varepsilon_{n_2} - \varepsilon_\nu - \varepsilon_{\mu_2}) (\varepsilon_{n_1} + \varepsilon_{n_2} - \varepsilon_{\mu_1} - \varepsilon_{\mu_2})}, \quad (\text{A14})$$

$$2 \sum_{\substack{\nu, \mu_1, \mu_2 > F \\ n_1, n_2 \leq F}} \sum_l \frac{2 \langle \varepsilon, n_2 | V_l | \mu_1, \nu \rangle \langle \mu_1, \mu_2 | V^{(l)} | n_1, n_2 \rangle \langle \nu, n_1 | \delta_l | \mu_2, \varepsilon \rangle}{(2l+1) (2l+1) (E + \varepsilon_{n_2} - \varepsilon_\nu - \varepsilon_{\mu_1}) (\varepsilon_{n_1} + \varepsilon_{n_2} - \varepsilon_{\mu_1} - \varepsilon_{\mu_2})}, \quad (\text{A15})$$

$$2 \sum_{\substack{\nu, \mu_1, \mu_2 > F \\ n_1, n_2 \leq F}} \sum_l \frac{2 \langle \varepsilon, n_2 | \delta_l | \mu_1, \nu \rangle \langle \mu_1, \mu_2 | V^{(l)} | n_1, n_2 \rangle \langle \nu, n_1 | V_l | \mu_2, \varepsilon \rangle}{(2l+1) (2l+1) (E + \varepsilon_{n_2} - \varepsilon_\nu - \varepsilon_{\mu_1}) (\varepsilon_{n_1} + \varepsilon_{n_2} - \varepsilon_{\mu_1} - \varepsilon_{\mu_2})}. \quad (\text{A16})$$

Appendix B: Numerical results

In order to facilitate comparison of the present calculations with future experimental and theoretical data we tabulate here the s -, p - and d -wave phase shifts, elastic scattering cross sections and s -, p -, d -wave Z_{eff} as a function of the incident positron momentum k for the noble gas sequence.

-
- [1] H. S. W. Massey and A. H. A. Moussa, Proc. Phys. Soc. London **71**, 38 (1958).
 - [2] C. M. Surko, G. F. Gribakin and S. J. Buckman, J. Phys. B **38** R57 (2005).
 - [3] V. B. Berestetskii, E. M. Lifshitz, and L. P. Pitaevskii, *Quantum Electrodynamics* (Pergamon, Oxford, 1982).
 - [4] I. Pomeranchuk, Zh. Eksp. Teor. Fiz. **19**, 183 (1949).
 - [5] V. I. Goldanskii and Y. S. Sayasov, Phys. Lett. **13**, 300 (1964).
 - [6] P. G. Coleman, T. C. Griffith, G. R. Heyland and T. L. Killeen, J. Phys. B **8**, 1734 (1975).
 - [7] T. J. Murphy, C. M. Surko, J. Phys. B **23**, L727 (1990).
 - [8] A preliminary account of these calculations is in J. Ludlow, PhD thesis, Queen's University Belfast, 2003.
 - [9] D. G. Green and G. F. Gribakin, *Enhancement and γ -spectra for positron annihilation on core and valence electrons*, to be submitted to Phys. Rev. A (2013).
 - [10] A. L. Fetter and J. D. Walecka, *Quantum Theory of Many-Particle Systems* (McGraw-Hill, New York, 1971).

TABLE III. Scattering phase shift δ_ℓ (in radians), elastic scattering cross section (10^{-16} cm²) and $Z_{\text{eff}}^{(\ell)}$ for ℓ -wave positrons annihilating on helium. Numbers in brackets denote powers of ten.

k (a.u.)	δ_s	δ_p	δ_d	σ	$Z_{\text{eff}}^{(s)}$	$Z_{\text{eff}}^{(p)}$	$Z_{\text{eff}}^{(d)}$
0.02	8.104[-3]	1.076[-4]	1.551[-5]	5.781[-1]	3.804[0]	1.297[-3]	1.490[-7]
0.04	1.514[-2]	4.176[-4]	6.444[-5]	5.053[-1]	3.788[0]	5.187[-3]	2.381[-6]
0.06	2.109[-2]	9.067[-4]	1.432[-4]	4.372[-1]	3.751[0]	1.167[-2]	1.203[-5]
0.08	2.606[-2]	1.568[-3]	2.483[-4]	3.776[-1]	3.709[0]	2.072[-2]	3.794[-5]
0.10	3.005[-2]	2.403[-3]	3.788[-4]	3.241[-1]	3.660[0]	3.233[-2]	9.235[-5]
0.20	3.716[-2]	8.784[-3]	1.500[-3]	1.430[-1]	3.375[0]	1.272[-1]	1.439[-3]
0.30	2.760[-2]	1.778[-2]	3.396[-3]	6.972[-2]	3.079[0]	2.764[-1]	6.976[-3]
0.40	6.907[-3]	2.795[-2]	6.093[-3]	5.775[-2]	2.808[0]	4.659[-1]	2.077[-2]
0.50	-2.074[-2]	3.795[-2]	9.585[-3]	7.501[-2]	2.569[0]	6.779[-1]	4.714[-2]
0.60	-5.235[-2]	4.667[-2]	1.380[-2]	1.023[-1]	2.363[0]	8.949[-1]	8.934[-2]
0.70	-8.564[-2]	5.340[-2]	1.868[-2]	1.298[-1]	2.186[0]	1.102[0]	1.512[-1]
0.80	-1.192[-1]	5.808[-2]	2.402[-2]	1.535[-1]	2.032[0]	1.297[0]	2.302[-1]
0.90	-1.519[-1]	6.043[-2]	2.972[-2]	1.717[-1]	1.902[0]	1.465[0]	3.366[-1]
1.00	-1.830[-1]	6.113[-2]	3.559[-2]	1.850[-1]	1.784[0]	1.625[0]	4.500[-1]

- [11] H. P. Kelly, Phys. Rev. **131**, 684 (1963).
- [12] M. Ya. Amusia, N. A. Cherepkov, L. V. Chernysheva, S. G. Shapiro and A. Tanchich, Pis'ma Zh. Eksp. Teor. Fiz. **68**, 2023 (1975); [Sov. Phys. JETP **41**, 1012 (1975)].
- [13] M. Ya. Amusia, N. A. Cherepkov, L. V. Chernysheva, D. M. Davidović and V. Radojević, Phys. Rev. A **25**, 219 (1982).
- [14] W. R. Johnson and C. Guet, Phys. Rev. A **49**, 1041 (1994); **64**, 019901 (2001).
- [15] *Many-body Atomic Physics*, edited by J. J. Boyle and M. S. Pindzola (Cambridge University Press, Cambridge, England, 1995).
- [16] M. Ya. Amusia, N. A. Cherepkov, L. V. Chernysheva, and S. G. Shapiro, J. Phys. B **9**, L531 (1976).
- [17] G. F. Gribakin and J. Ludlow, Phys. Rev. A **70**, 032720 (2004).

TABLE IV. Scattering phase shift δ_ℓ , elastic scattering cross section and $Z_{\text{eff}}^{(\ell)}$ for ℓ -wave positrons on neon. Numbers in brackets denote powers of ten.

k (a.u.)	Phase shift (rad.)			Cross Section (10^{-16} cm 2)	$Z_{\text{eff}}^{(s)}$		$Z_{\text{eff}}^{(p)}$		$Z_{\text{eff}}^{(d)}$	
	δ_s	δ_p	δ_d		σ	n^{a}	$(n-1)^{\text{b}}$	n^{a}	$(n-1)^{\text{b}}$	n^{a}
0.02	8.201[-3]	2.081[-4]	3.099[-5]	5.929[-1]	5.590[0]	1.612[-2]	3.380[-3]	1.671[-6]	4.275[-7]	7.000[-8]
0.04	1.443[-2]	7.891[-4]	1.254[-4]	4.622[-1]	5.549[0]	1.602[-2]	1.353[-2]	4.674[-6]	6.834[-6]	1.122[-7]
0.06	1.873[-2]	1.691[-3]	2.759[-4]	3.517[-1]	5.465[0]	1.579[-2]	3.043[-2]	1.053[-5]	3.455[-5]	5.688[-6]
0.08	2.133[-2]	2.902[-3]	4.735[-4]	2.648[-1]	5.371[0]	1.555[-2]	5.408[-2]	1.876[-5]	1.090[-4]	1.734[-5]
0.10	2.229[-2]	4.421[-3]	7.147[-4]	1.966[-1]	5.265[0]	1.523[-2]	8.441[-2]	2.936[-5]	2.653[-4]	4.321[-5]
0.16 ^c	1.652[-2]	1.067[-2]	1.773[-3]	8.725[-2]	—	—	—	—	—	—
0.18 ^c	1.211[-2]	1.320[-2]	2.253[-3]	7.628[-2]	—	—	—	—	—	—
0.20	6.652[-3]	1.592[-2]	2.792[-3]	7.522[-2]	4.695[0]	1.387[-2]	3.314[-1]	1.178[-4]	4.141[-3]	7.000[-4]
0.22 ^c	2.191[-4]	1.880[-2]	3.384[-3]	8.245[-2]	—	—	—	—	—	—
0.24 ^c	-7.089[-3]	2.181[-2]	4.035[-3]	9.668[-2]	—	—	—	—	—	—
0.30	-3.347[-2]	3.130[-2]	6.383[-3]	1.689[-1]	4.169[0]	1.268[-2]	7.122[-1]	2.626[-4]	2.005[-2]	3.500[-2]
0.40	-8.843[-2]	4.692[-2]	1.155[-2]	3.354[-1]	3.729[0]	1.180[-2]	1.174[0]	4.549[-4]	5.955[-2]	1.122[-1]
0.50	-1.520[-1]	5.943[-2]	1.824[-2]	5.014[-1]	3.368[0]	1.120[-2]	1.656[0]	6.817[-4]	1.344[-1]	2.700[-1]
0.60	-2.200[-1]	6.655[-2]	2.618[-2]	6.378[-1]	3.074[0]	1.084[-2]	2.107[0]	9.297[-4]	2.529[-1]	5.600[-1]
0.70	-2.897[-1]	6.700[-2]	3.503[-2]	7.390[-1]	2.834[0]	1.066[-2]	2.492[0]	1.191[-3]	4.248[-1]	1.000[-1]
0.80	-3.597[-1]	6.093[-2]	4.406[-2]	8.119[-1]	2.632[0]	1.065[-2]	2.810[0]	1.461[-3]	6.338[-1]	1.700[-1]
0.90	-4.283[-1]	4.851[-2]	5.289[-2]	8.612[-1]	2.469[0]	1.079[-2]	3.034[0]	1.733[-3]	9.162[-1]	2.800[-1]
1.00	-4.947[-1]	3.134[-2]	6.080[-2]	8.938[-1]	2.326[0]	1.105[-2]	3.236[0]	2.011[-3]	1.187[0]	4.000[-1]

^a Total for annihilation on valence n shell ($3s + 3p$ subshell total).

^b Total for annihilation on core $(n-1)$ shell ($2s + 2p$ subshell total), from Ref. [9].

^c Values given to allow the accurate reproduction of the minimum in the elastic scattering cross-section.

Z_{eff} values for these positron momenta can be requested from the authors.

TABLE V. Scattering phase shift δ_ℓ , elastic scattering cross section and $Z_{\text{eff}}^{(\ell)}$ for ℓ -wave positrons on argon. Numbers in brackets denote powers of ten.

k (a.u.)	Phase shift (rad.)			Cross Section (10^{-16} cm 2)	$Z_{\text{eff}}^{(s)}$		$Z_{\text{eff}}^{(p)}$		$Z_{\text{eff}}^{(d)}$	
	δ_s	δ_p	δ_d		σ	n^a	$(n-1)^b$	n^a	$(n-1)^b$	n^a
0.02	8.178[-2]	8.777[-4]	1.275[-4]	5.873[1]	2.865[1]	1.653[-1]	1.992[-2]	3.397[-5]	4.288[-6]	9.62[-7]
0.04	1.502[-1]	3.453[-3]	5.099[-4]	4.933[1]	2.698[1]	1.558[-1]	8.007[-2]	1.368[-4]	6.858[-5]	1.5[-6]
0.06	2.011[-1]	7.673[-3]	1.132[-3]	3.918[1]	2.432[1]	1.407[-1]	1.812[-1]	3.104[-4]	3.469[-4]	7.8[-5]
0.08	2.374[-1]	1.356[-2]	1.980[-3]	3.073[1]	2.176[1]	1.261[-1]	3.239[-1]	5.569[-4]	1.094[-3]	2.4[-4]
0.10	2.604[-1]	2.112[-2]	3.060[-3]	2.382[1]	1.935[1]	1.126[-1]	5.083[-1]	8.782[-4]	2.665[-3]	6.0[-4]
0.20	2.539[-1]	7.964[-2]	1.291[-2]	7.312[0]	1.146[1]	6.873[-2]	1.998[0]	3.589[-3]	4.149[-2]	9.9[-3]
0.30	1.534[-1]	1.548[-1]	3.096[-2]	3.928[0]	7.754[0]	4.900[-2]	3.995[0]	7.632[-3]	1.988[-1]	5.1[-2]
0.40	2.149[-2]	2.172[-1]	5.835[-2]	3.518[0]	5.785[0]	3.929[-2]	5.670[0]	1.176[-2]	5.753[-1]	1.6[-1]
0.50	-1.195[-1]	2.484[-1]	9.424[-2]	3.484[0]	4.608[0]	3.424[-2]	6.595[0]	1.510[-2]	1.240[0]	4.0[-1]
0.60	-2.603[-1]	2.464[-1]	1.352[-1]	3.437[0]	3.834[0]	3.165[-2]	6.887[0]	1.770[-2]	2.183[0]	7.9[-1]
0.70	-3.966[-1]	2.181[-1]	1.773[-1]	3.410[0]	3.306[0]	3.066[-2]	6.818[0]	1.976[-2]	3.332[0]	1.5[-1]
0.80	-5.273[-1]	1.732[-1]	2.175[-1]	3.440[0]	2.916[0]	3.068[-2]	6.601[0]	2.217[-2]	4.673[0]	2.2[-1]

^a Total for annihilation on valence n shell ($3s + 3p$ subshell total).

^b Total for annihilation on core $(n-1)$ shell ($2s + 2p$ subshell total), from Ref. [9].

- [19] A. R. Tančić, M. Ya. Amusia, N. K. Cherepkov and M. R. Nikolić, Phys. Lett. A **140**, 503 (1989).
- [20] M. R. Nikolić and A. R. Tančić, Facta Universitatis: Physics, Chemistry and Technology **3** 141 (2005)
- [21] G. F. Gribakin and W. A. King, J. Phys. B **27**, 2639 (1994).
- [22] V. A. Dzuba, V. V. Flambaum, G. F. Gribakin, and W. A. King, Phys. Rev. A **52**, 4541 (1995).
- [23] V. A. Dzuba, V. V. Flambaum, G. F. Gribakin, and W. A. King, J. Phys. B **29**, 3151 (1996).
- [24] G. F. Gribakin and W. A. King, Can. J. Phys. **74**, 449 (1996).

TABLE VI. Scattering phase shift δ_ℓ , elastic scattering cross section and $Z_{\text{eff}}^{(\ell)}$ for ℓ -wave positrons on krypton. Numbers in brackets denote powers of ten.

k (a.u.)	Phase shift (rad.)			Cross Section (10^{-16} cm 2)	$Z_{\text{eff}}^{(s)}$		$Z_{\text{eff}}^{(p)}$		$Z_{\text{eff}}^{(d)}$
	δ_s	δ_p	δ_d	σ	n^a	$(n-1)^b$	n^a	$(n-1)^b$	n^a
0.02	1.812[-1]	1.378[-3]	1.990[-4]	2.858[2]	8.419[1]	1.362[0]	3.939[-2]	2.438[-4]	9.621[-6]
0.04	3.228[-1]	5.454[-3]	7.932[-4]	2.215[2]	7.112[1]	1.150[0]	1.589[-1]	9.855[-4]	1.539[-4]
0.06	4.114[-1]	1.223[-2]	1.757[-3]	1.568[2]	5.573[1]	9.007[-1]	3.615[-1]	2.249[-3]	7.788[-4]
0.08	4.639[-1]	2.184[-2]	3.065[-3]	1.109[2]	4.394[1]	7.108[-1]	6.500[-1]	4.061[-3]	2.458[-3]
0.10	4.885[-1]	3.436[-2]	4.731[-3]	7.880[1]	3.509[1]	5.691[-1]	1.026[0]	6.444[-3]	5.990[-3]
0.20	4.269[-1]	1.338[-1]	2.038[-2]	2.000[1]	1.526[1]	2.556[-1]	4.045[0]	2.657[-2]	9.364[-2]
0.30	2.631[-1]	2.560[-1]	5.050[-2]	1.075[1]	9.063[0]	1.610[-1]	7.527[0]	5.293[-2]	4.501[-1]
0.40	7.878[-2]	3.399[-1]	9.779[-2]	8.678[0]	6.318[0]	1.219[-1]	9.384[0]	7.220[-2]	1.294[0]
0.50	-1.053[-1]	3.625[-1]	1.596[-1]	7.492[0]	4.831[0]	1.031[-1]	9.584[0]	8.203[-2]	2.718[0]
0.60	-2.826[-1]	3.352[-1]	2.273[-1]	6.774[0]	3.915[0]	9.391[-2]	9.020[0]	8.751[-2]	4.548[0]
0.70	-4.493[-1]	2.777[-1]	2.933[-1]	6.463[0]	3.309[0]	9.096[-2]	8.316[0]	9.098[-2]	6.627[0]

^a Total for annihilation on valence n shell ($4s + 4p$ subshell total).

^b Total for annihilation on core $(n-1)$ shell ($3s + 3p + 3d$ subshell total), from Ref. [9].

- [25] V. A. Dzuba, V. V. Flambaum, W. A. King, B. N. Miller, and O. P. Sushkov, *Phys. Scr.* **T46**, 248 (1993).
- [26] L. J. M. Dunlop and G. F. Gribakin, *Nucl. Instr. Methods B* **247**, 61 (2006).
- [27] J. A. Ludlow and G. F. Gribakin, *International Review of Atomic and Molecular Physics*, **1**(1), January-June, 73 (2010).
- [28] D. G. Green and G. F. Gribakin, *Phys. Rev. A* **88**, 032708 (2013).
- [29] L. J. M. Dunlop and G. F. Gribakin, *J. Phys. B* **39**, 1647 (2006).
- [30] D. G. Green, S. Saha, F. Wang, G. F. Gribakin, and C. M. Surko, *New J. Phys* **14**, 035021 (2012).

TABLE VII. Scattering phase shift δ_ℓ , elastic scattering cross section and $Z_{\text{eff}}^{(\ell)}$ for ℓ -wave positrons on xenon. Numbers in brackets denote powers of ten.

k (a.u.)	Phase shift (rad.)			Cross Section (10^{-16} cm 2)	$Z_{\text{eff}}^{(s)}$		$Z_{\text{eff}}^{(p)}$		$Z_{\text{eff}}^{(d)}$
	δ_s	δ_p	δ_d	σ	n^{a}	$(n-1)^{\text{b}}$	n^{a}	$(n-1)^{\text{b}}$	n^{a}
0.02	9.849[-1]	2.303[-3]	3.223[-4]	6.108[3]	1.227[3]	2.971[1]	1.040[-1]	1.085[-3]	2.716[-5]
0.04	1.151[0]	9.418[-3]	1.285[-3]	1.835[3]	3.517[2]	8.289[0]	4.235[-1]	4.428[-3]	4.350[-4]
0.06	1.130[0]	2.178[-2]	2.856[-3]	8.010[2]	1.610[2]	3.767[0]	9.763[-1]	1.025[-2]	2.205[-3]
0.08	1.085[0]	4.001[-2]	5.015[-3]	4.327[2]	9.391[1]	2.195[0]	1.782[0]	1.880[-2]	6.975[-3]
0.10	1.027[0]	6.450[-2]	7.809[-3]	2.622[2]	6.239[1]	1.463[0]	2.854[0]	3.032[-2]	1.704[-2]
0.20	7.199[-1]	2.666[-1]	3.572[-2]	5.723[1]	1.888[1]	4.608[-1]	1.122[1]	1.256[-1]	2.713[-1]
0.30	4.256[-1]	4.784[-1]	9.425[-2]	3.349[1]	1.001[1]	2.623[-1]	1.675[1]	2.023[-1]	1.325[0]
0.40	1.551[-1]	5.624[-1]	1.904[-1]	2.365[1]	6.618[0]	1.912[-1]	1.584[1]	2.110[-1]	3.769[0]
0.50	-9.220[-2]	5.354[-1]	3.118[-1]	1.839[1]	4.906[0]	1.597[-1]	1.328[1]	1.989[-1]	7.384[0]
0.60	-3.192[-1]	4.503[-1]	4.298[-1]	1.595[1]	3.896[0]	1.453[-1]	1.108[1]	1.896[-1]	1.099[1]

^a Total for annihilation on valence n shell ($5s + 5p$ subshell total).

^b Total for annihilation on core $(n-1)$ shell ($4s + 4p + 4d$ subshell total), from Ref. [9].

- [31] V. A. Dzuba, V. V. Flambaum, G. F. Gribakin, and C. Harabati, Phys. Rev. A **86**, 032503 (2012).
- [32] C. Harabati, V. A. Dzuba, and V. V. Flambaum, Phys. Rev. A **89**, 022517 (2014).
- [33] J. P. Sullivan, C. Makochekanwa, A. Jones, P. Caradonna and S. J. Buckman, J. Phys. B **41** 081001 (2008).
- [34] A. Zecca, L. Chiari, E. Trainotti, D. V. Fursa, I. Bray, and M. J. Brunger, Eur. Phys. J. D **64**, 317 (2011).
- [35] A. Zecca, L. Chiari, E. Trainotti, D. V. Fursa, I. Bray, A Sarkar, S Chattopadhyay, K Ratanavelu, and M. J. Brunger, J. Phys. B **45** 015203 (2012).
- [36] A. Zecca, L. Chiari, E. Trainotti, and M. J. Brunger, J. Phys. B **45** 085203 (2012).

- [37] C. Makochekeanwa, J. R. Machacek, A. C. L. Jones, P. Caradonna, D. S. Slaughter, R. P. McEachran, J. P. Sullivan, S. J. Buckman, S. Bellm, B. Lohmann, D. V. Fursa, I. Bray, D. W. Mueller, A. D. Stauffer, and M. Hoshino, *Phys. Rev. A* **83**, 032701 (2011).
- [38] C. Makochekeanwa, J. R. Machacek, A. C. L. Jones, P. Caradonna, D. S. Slaughter, R. P. McEachran, J. P. Sullivan, S. J. Buckman, S. Bellm, B. Lohmann, D. V. Fursa, I. Bray, D. W. Mueller, A. D. Stauffer, and M. Hoshino, *Phys. Rev. A* **83**, 032721 (2011).
- [39] J. R. Machacek, C. Makochekeanwa, A. C. L. Jones, P. Caradonna, D. S. Slaughter, R. P. McEachran, J. P. Sullivan, S. J. Buckman, S. Bellm, B. Lohmann, D. V. Fursa, I. Bray, D. W. Mueller, and A. D. Stauffer, *New J. Phys.* **13** 125004 (2011).
- [40] D. V. Fursa and I. Bray, *New J. Phys.* **14**, 035002 (2012).
- [41] A. B. Migdal, *Theory of Finite Fermi-Systems and Applications to Atomic Nuclei* (Interscience, New York, 1967).
- [42] J. S. Bell and E. J. Squires, *Phys. Rev. Lett.* **3**, 96 (1959).
- [43] M. Ya. Amusia and N. A. Cherepkov, *Case Studies in Atomic Physics* **5**, 47 (1975).
- [44] See also Ref. [13]; in this paper the self-energy operator Σ_E is expressed in Rydberg and the coefficient in Eq. (9) is $-\pi$.
- [45] P. A. Fraser, *Adv. At. Mol. Phys.* **4**, 63 (1968).
- [46] M. Ya. Amusia and L. V. Chernysheva, *Computation of Atomic Processes. A Handbook for the ATOM Programs* (IOP Publishing, Bristol, 1997).
- [47] C. De. Boor, *A Practical guide to Splines* (Springer, New York, 1978).
- [48] J. Sapirstein and W. R. Johnson, *J. Phys. B* **29**, 5213 (1996).
- [49] G. F. Gribakin and J. Ludlow, *J. Phys. B* **35**, 339 (2002).
- [50] T. F. O'Malley, L. Spruch, and L. Rosenberg, *J. Math. Phys.* **2**, 491 (1961).
- [51] L. D. Landau and E. M. Lifshitz, *Quantum Mechanics*, 3rd ed. (Pergamon, Oxford, 1977).
- [52] R. P. McEachran, D. L. Morgan, A. G. Ryman, and A. D. Stauffer, *J. Phys. B* **10**, 663 (1977); **11**, 951 (1978), R. P. McEachran, A. G. Ryman, and A. D. Stauffer, *J. Phys. B* **11**, 551 (1978); **12**, 1031 (1979), R. P. McEachran, A. D. Stauffer, and L. E. M. Campbell, *J. Phys. B* **13**, 1281 (1980).
- [53] R. I. Campeanu and J. W. Humberston *J. Phys. B* **10** L153 (1977)
- [54] P. Van Reeth and J. W. Humberston, *J. Phys. B* **32**, 3651 (1999).
- [55] H. Wu, I. Bray, D. V. Fursa, and A. T. Stelbovics, *J. Phys. B* **37** L1 (2004).

- [56] T. S. Stein, W. E. Kauppila, V. Pol, J. H. Smart, and G. Jesion, *Phys. Rev. A* **17**, 1600 (1978).
- [57] T. Mizogawa, Y. Nakayama, T. Kawaratani, and M. Tosaki, *Phys. Rev. A* **31**, 2171 (1985).
- [58] P. M. Jay and P. G. Coleman, *Phys. Rev. A* **82**, 012701 (2010).
- [59] G. Sinapius, W. Raith, and W. G. Wilson, *J. Phys. B* **13**, 4079 (1980).
- [60] S. P. Parikh, W. E. Kauppila, C. K. Kwan, R. A. Lukaszew, D. Przybyla, T. S. Stein, and S. Zhou, *Phys. Rev. A* **47**, 1535 (1993).
- [61] W. E. Kauppila, T. S. Stein, and G. Jesion, *Phys. Rev. Lett.* **36**, 580 (1976).
- [62] M. S. Dababneh, W. E. Kauppila, J. P. Downing, F. Laperriere, V. Pol, J. H. Smart, and T. S. Stein, *Phys. Rev. A* **22**, 1872 (1978).
- [63] S. J. Gilbert, R. G. Greaves, and C. M. Surko, *Phys. Rev. Lett.* **82**, 5032 (1999).
- [64] J. P. Marler, C. M. Surko, R. P. McEachran, and A. D. Stauffer, *Phys. Rev. A* **73**, 064702 (2006).
- [65] L. T. Sin Fai Lam, *J. Phys. B* **15**, 143 (1982).
- [66] P. Van Reeth, J. W. Humberston, K. Iwata, R. G. Greaves, and C. M. Surko, *J. Phys. B* **29** L465 (1996).
- [67] G. L. Wright, M. Charlton, T. C. Griffith, and G. R. Heyland, *J. Phys. B* **18**, 4327 (1985).
- [68] K. Iwata, R. G. Greaves, T. J. Murphy, M. D. Tinkle, and C. M. Surko, *Phys. Rev. A* **51**, 473 (1995).
- [69] V. A. Dzuba, V. V. Flambaum, P. G. Silvestrov, and O. P. Sushkov, *Phys. Lett. A* **131**, 461 (1988).
- [70] V. A. Dzuba, V. V. Flambaum, and O. P. Sushkov, *Phys. Lett. A* **140**, 493 (1989).
- [71] M. J. Puska and R. M. Nieminen, *Rev. Mod. Phys.* **66**, 841 (1994).
- [72] D. A. Varshalovich, A. N. Moskalev, and V. K. Khersonskii, *Quantum Theory of Angular Momentum* (World Scientific, Singapore, 1988).
- [73] K. Nagumo, Y. Nitta, M. Hoshino, H. Tanaka, and Y. Nagashima, *J. Phys. Soc. Jpn.* **80**, 064301 (2011); *ibid.* **80**, 098001 (2011).
- [74] K. Nagumo, Y. Nitta, M. Hoshino, H. Tanaka, and Y. Nagashima, *Eur. Phys. J. D* **66**, 81 (2012).
- [75] G. P. Karwasz, D. Pliszka, A. Zecca and R. S. Brusa, *Nucl. Instrum. Methods B* **240**, 666 (2005).

[76] G. P. Karwasz, D. Pliszka and R. S. Brusa, Nucl. Instrum. Methods B **247**, 68 (2006).